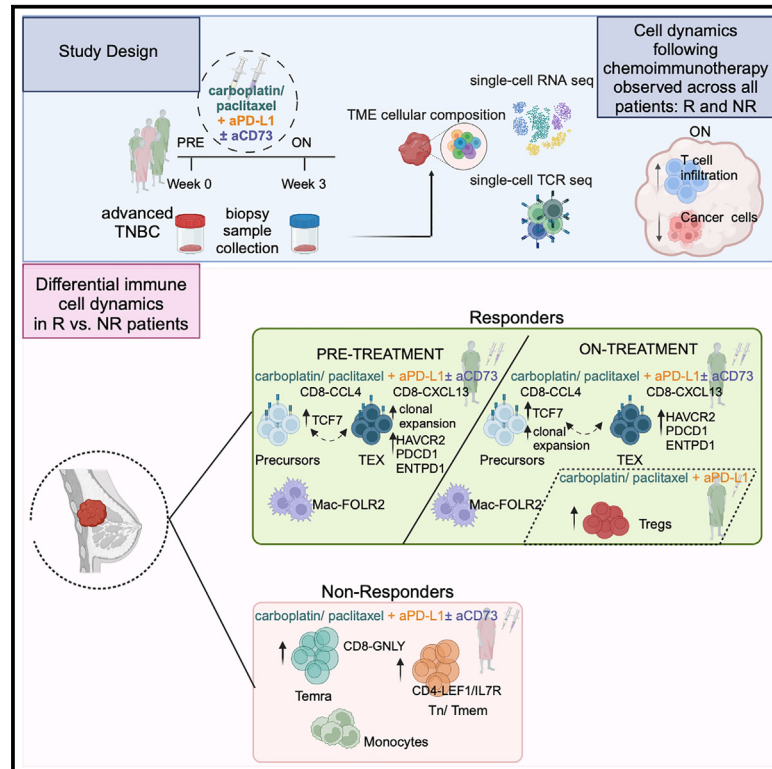


Continuous replenishment of the dysfunctional CD8 T cell axis is associated with response to chemoimmunotherapy in advanced breast cancer

Graphical abstract



Authors

Christina Metoikidou, Vadim Karnaukhov, Bram Boeckx, ..., Diether Lambrechts, Sebastian Amigorena, Emanuela Romano

Correspondence

emanuela.romano@curie.fr

In brief

Using single-cell profiling, Metoikidou et al. study chemoimmunotherapy in metastatic triple-negative breast cancer. Enrichment in clonally expanded, dysfunctional CD8 cells is observed in responders, while non-responders display increased fractions of terminal effector-memory CD8 cells. These findings highlight the role of T cell clonal dynamics in predicting and assessing treatment response.

Highlights

- High TCR clonality in late-dysfunctional CD8 T cells predicts chemoimmunotherapy response
- Early-dysfunctional CD8 T cell expansions occur in responders on treatment
- Responders show both clonal replacement and reinvigoration on treatment
- Temra CD8 T cell enrichment in non-responders on treatment

Article

Continuous replenishment of the dysfunctional CD8 T cell axis is associated with response to chemoimmunotherapy in advanced breast cancer

Christina Metoikidou,^{1,2} Vadim Karnaukhov,^{1,3} Bram Boeckx,^{4,5} Eleonora Timperi,¹ Pierre-Emmanuel Bonté,¹ Ling Wang,^{4,5} Marion Espenel,⁶ Benoit Albaud,⁶ Delphine Loirat,⁷ Xiaoxiao Wang,⁸ Christos Sotiriou,⁸ Philippe Aftimos,⁸ Kevin Punie,^{9,10} Hans Wildiers,^{9,10} Viktorija Labroska,^{11,12} Ming-Wei Wang,^{11,12} Joshua J. Waterfall,^{13,14} Martine Piccart-Gebhart,⁸ Thierry Mora,³ Aleksandra Walczak,³ Olivier Lantz,^{1,15,16} Laurence Buisseret,⁸ Diether Lambrechts,^{4,5,17} Sebastian Amigorena,^{1,17} and Emanuela Romano^{1,7,17,18,*}

¹Institut Curie, PSL University, Inserm U932, Immunity and Cancer, 75005 Paris, France

²Division of Molecular Oncology and Immunology, The Netherlands Cancer Institute, Amsterdam, the Netherlands

³Laboratoire de Physique de l'École Normale Supérieure, Paris Sciences & Lettres University, CNRS, Sorbonne Université and Université Paris Cité, 75005 Paris, France

⁴Laboratory for Translational Genetics, Department of Human Genetics, KU Leuven, Leuven, Belgium

⁵VIB Center for Cancer Biology, Leuven, Belgium

⁶Institut Curie Genomics of Excellence (ICGex) Platform, Institut Curie, 75005 Paris, France

⁷Department of Medical Oncology, Center for Cancer Immunotherapy, Institut Curie, Paris, France

⁸Institut Jules Bordet, Université Libre de Bruxelles, Brussels, Belgium

⁹Department of General Medical Oncology and Multidisciplinary Breast Centre, Leuven Cancer Institute, Leuven, Belgium

¹⁰University Hospitals Leuven, Leuven, Belgium

¹¹The National Center for Drug Screening, Shanghai Institute of Materia Medica, Chinese Academy of Sciences (CAS), Shanghai, China

¹²University of Chinese Academy of Sciences, Beijing 100049, China

¹³Translational Research Department, Institut Curie, 75005 Paris, France

¹⁴INSERM U830, Institut Curie, 75005 Paris, France

¹⁵Laboratoire d'immunologie clinique, Institut Curie, 75005 Paris, France

¹⁶Centre d'investigation Clinique en Thérapie Gustave-Roussy Institut Curie (CIC-BT1428), Paris, France

¹⁷These authors contributed equally

¹⁸Lead contact

*Correspondence: emanuela.romano@curie.fr

<https://doi.org/10.1016/j.xcrm.2025.101973>

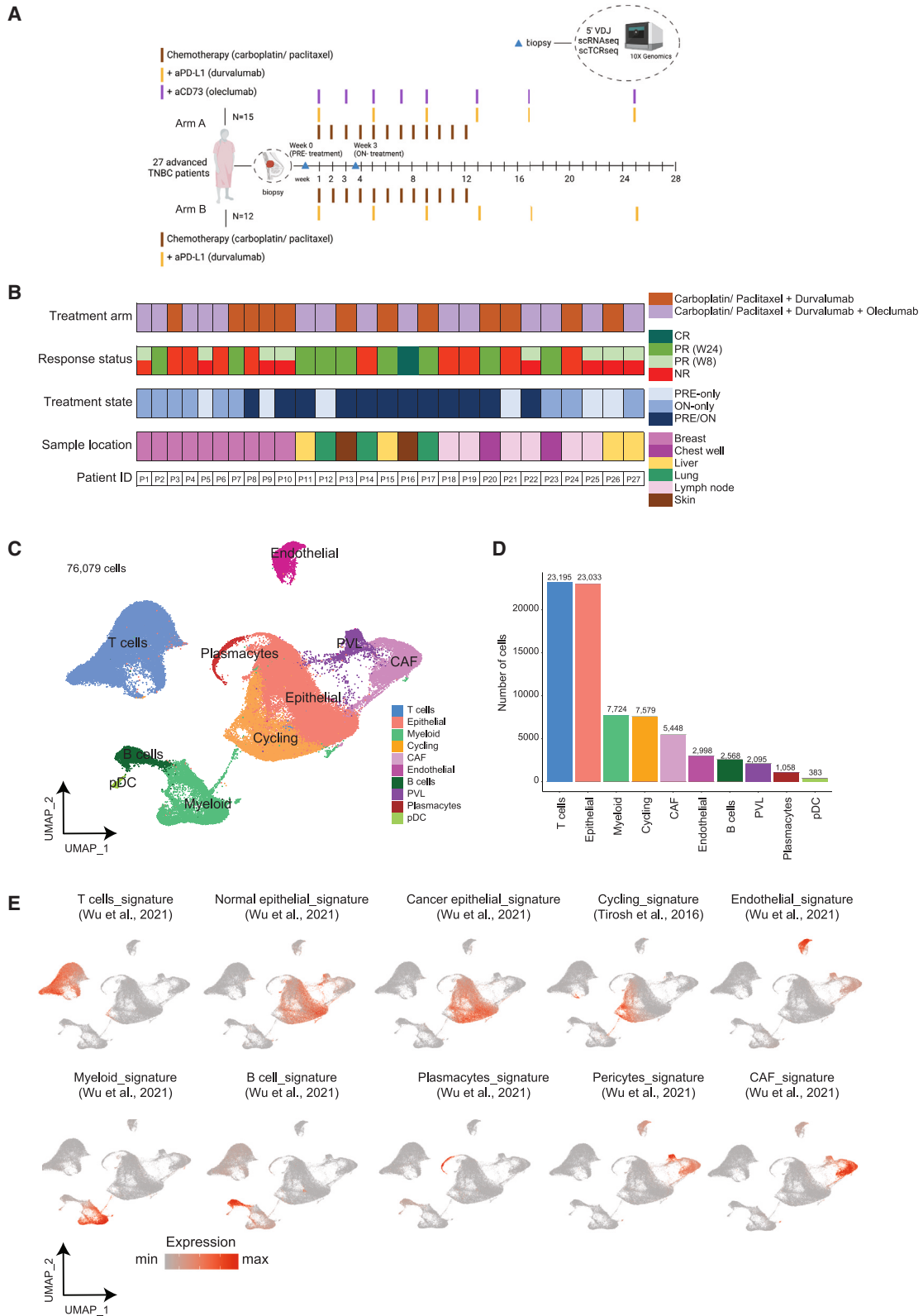
SUMMARY

Chemotherapy combined with immune checkpoint blockade has shown clinical activity in breast cancer. Response, however, occurs in only a low proportion of patients. How the immune landscape of the tumor determines the immune and clinical responses to chemoimmunotherapy is not well understood. Here, using a combination of single-cell RNA sequencing (scRNA-seq) and single-cell T cell receptor sequencing (scTCR-seq), we profile 40 biopsies from 27 patients with metastatic triple-negative breast cancer (TNBC), receiving chemotherapy and anti-PD-L1 alone or in combination with anti-CD73, in a phase 2 randomized clinical trial. Our results show an enrichment of late-dysfunctional, clonally expanded CD8⁺ T cells in responder (R) patients. On treatment, R display an influx of newly emerging clonotypes, as well as expansion of the CD8⁺ precursors. Collectively, our data suggest that baseline clonal expansion could be a potential predictor of response and that both clonal reinvigoration of pre-existing tumor-reactive T cells and clonal replacement on-treatment are important for a protective response to chemoimmunotherapy.

INTRODUCTION

Breast cancer (BC) is the second cause of cancer death in women, worldwide.¹ Triple-negative BC (TNBC) represents 10%–15% of all BC cases, and it is highly heterogeneous and aggressive with rather poor prognosis.² Chemotherapy, radiation, and surgery have long been the primary treatments for TNBC, but recent advances have introduced novel therapies, including PARP inhibitors³ and antibody-drug conjugates.^{4,5}

TNBC is more enriched in tumor-infiltrating lymphocytes (TILs) compared to hormone-receptor-positive BC tumors, suggesting that patients with TNBC could benefit from immune checkpoint blockade (ICB).⁶ Recent studies show promising results for aPD-1/PD-L1 as monotherapy or in combination with chemotherapy, in improving progression-free survival and overall survival (OS) rates.⁷ In patients with PD-L1⁺ metastatic TNBC, the PD-L1 blocking antibody pembrolizumab, combined with nab-paclitaxel, improves patients' OS rate.⁸ To further improve the



(legend on next page)

clinical outcomes, novel immunotherapy targets are being explored.

CD73, an ecto-5'-nucleotidase involved in adenosine (ADO) metabolism, has emerged as a potential therapeutic target.⁹ Elevated ADO levels in the hypoxic tumor microenvironment (TME) activate the A2A receptor on T cells, suppressing immune functions.^{10–12} CD73 is upregulated in solid tumors, such as ovarian cancer and BC,¹³ with recent findings showing that CD73 is involved in cellular adhesion and angiogenesis, supporting metastasis and cancer progression.¹⁴ Particularly in TNBC, recent studies have highlighted the role of CD73 in resistance to chemotherapy and poor prognosis.^{15,16} In combination with PD-1/PD-L1 blockade, anti-CD73 therapy has shown promise in other cancer types, such as EGFR-mutant non-small cell lung cancer, by enhancing anti-tumor immune responses.¹⁷ Thus, blocking CD73 in combination with PD-1/PD-L1 blockade is considered a rational therapeutic approach.

CD8⁺ T cell infiltration in tumors is generally linked to better clinical outcomes,¹⁸ but these cells are highly heterogeneous. Recent advances in single-cell transcriptomics have revealed distinct states, including memory-like precursors (showing increased expression of markers such as *TCF1* and *IL7R*) and late-dysfunctional CD8⁺ T cells (showing increased expression of markers such as *TOX*, *PDCD1*, *HAVCR2*, *LAG3*, and *ENTPD1*) in human tumors.^{19–21} How these states are associated with response to treatment is a central, open question. Recent studies in melanoma showed that memory precursor CD8⁺ T cells are critical for tumor control in response to ICB.^{22,23} On the other hand, in non-small cell lung cancer, tissue-resident CD8⁺ T cells expressing exhaustion markers (*HAVCR2/TIM3*, *PDCD1/PD-1*, and *ENTPD1/CD39*) correlate with improved disease prognosis,²⁴ highlighting the tumor-reactive properties of this subset. Similar findings in early-stage BC²⁵ suggest that the presence of tissue-resident exhausted CD8⁺ T cells correlates with clinical responses to aPD-1 therapy.

Here, we used a combination of single-cell RNA sequencing (scRNA-seq) and single-cell T cell receptor sequencing (scTCR-seq) to analyze immune cell dynamics in patients with advanced TNBC treated with chemotherapy (carboplatin/paclitaxel) and anti-PD-L1 (durvalumab), with or without anti-CD73 (oleclumab), as first-line therapy in a phase 2 randomized clinical trial (NCT03616886). Our results suggest that an increased fraction and clonal expansion of late-dysfunctional CD8⁺ T cells, prior to treatment, are associated with clinical response. Upon treatment, responder patients show higher fractions of new emerging clonotypes together with expansion of the precursor CD8⁺ T cell pool. These results suggest that the reinvigora-

tion of pre-existing late-dysfunctional CD8⁺ T cell clones, the emergence of new clonotypes, and the expansion of dysfunctional precursor CD8⁺ T cell clones upon treatment collectively contribute to objective clinical responses to chemoimmunotherapy in BC. This underscores the critical role of this dual mechanism of clonal reactivation and replacement in driving positive clinical outcomes.

RESULTS

Transcriptomic landscape of metastatic TNBC

In the SYNERGY clinical trial, patients with advanced metastatic TNBC receiving first-line therapy were randomized into two treatment arms. Arm A combined chemotherapy (carboplatin/paclitaxel) with anti-PD-L1 (durvalumab) plus anti-CD73 (oleclumab); arm B combined chemotherapy with anti-PD-L1. A total of 40 biopsy samples were collected PRE-treatment (baseline/week 0) and ON-treatment (week 3) from 27 patients, including 12 patients with paired samples (PRE- and ON-treatment) (Figures 1A and 1B; Figure S1A; Table S1). Biopsies were obtained from either primary tumor tissue ($n = 10$) or metastatic sites ($n = 17$) (Figure 1B). For $n = 9$ patients, biopsy samples were collected ON-treatment only, and for $n = 6$ patients, biopsy samples were collected PRE-treatment only.

Clinical outcomes were assessed using response evaluation criteria in solid tumors (RECIST)²⁶ at week 24 (Figure 1B). Responders (R, $n = 10$) included nine with partial response (PR) and one with complete response. Two patients had stable disease, and 17 were non-responders (NRs). Among NRs, eight initially showed PR at week 8 but progressed by week 24 (short-lived R), and nine showed progressive disease by week 8 (Figure 1B; Table S 1).

Tissue samples were enzymatically dissociated, and tumor-infiltrating cells, including immune, stromal, and tumor cells, were analyzed using paired scRNA-seq and scTCR-seq via 5'/VDJ 10X Genomics technology. Batch effects across patients (Figures S1B and S1C) and tissues (Figures S1D and S1E) were removed through data integration, yielding high-quality transcriptome data for 76,079 single cells (Figure 1C). Clustering via uniform manifold approximation and projection (UMAP) and graph-based methods identified 10 cell clusters based on their transcriptome profiles. Differential expression (DE) analysis (Figure 1C; Figure S1F; Table S2) and cell type-specific gene signatures^{27,28} (Figure 1E; Table S3) revealed major clusters, including T cells, epithelial cells (normal and cancer), endothelial cells, cancer-associated fibroblasts (CAFs), pericytes, myeloid cells, B cells, and plasmacytes. Cycling cells cluster together due to

Figure 1. Study design and profiling of immune and non-immune cell types in metastatic TNBC

(A) Overview of study design for biopsy analysis in patients with metastatic TNBC. Biopsy samples ($n = 40$) from 27 patients were collected at two time points: PRE-treatment (baseline/week 0) and/or ON-treatment (week 3), across two arms: chemotherapy + aPD-L1 (arm B, $n = 12$) or chemotherapy + aPD-L1 + aCD73 (arm A, $n = 15$). Created with BioRender.com.

(B) Clinical metadata, including treatment arm, RECIST-based response metrics, time point, and sample tissue origin. Combined red/green response status indicates short-lived responders.

(C) UMAP representation of 76,079 tumor-infiltrating cells, color-coded by cell population. pDC: plasmacytoid dendritic cell; PVL, perivascular cell; CAFs, cancer-associated fibroblasts.

(D) Distribution of cell numbers per cluster.

(E) Normalized expression of a selected set of gene signatures, demonstrating cell type identities.

co-expression of cell cycle genes, distinctive of G2/M and S cycling phase.²⁷

All clusters were represented across samples (Figure S1C) and tissue types (Figure S1E), though CAFs were more abundant in chest wall biopsies, and B cells were enriched in lymph node biopsies (Figure S1E). Epithelial cells and T cells were the most abundant clusters (Figure 1D). These findings illuminate the immune-infiltrated TNBC landscape, providing a basis for further analysis.

Immune and non-immune cell dynamics PRE- vs. ON-treatment

To identify populations affected by treatment, we compared cluster distributions in PRE- and ON-treatment biopsy samples. PRE-treatment biopsies are enriched in epithelial cells, while ON-treatment biopsies show higher T cell density (Figure 2A). Upon treatment, there is a global increase in T cell populations and a reduction in epithelial cells (Figure 2B), observed in almost all patients (Figure 2C). No significant changes were noted in other cell populations between PRE- and ON-treatment (Figure S2A).

Comparing transcriptomic profiles of R and NRs (evaluated at week 24), we observed consistent T cell expansion and epithelial cell reduction upon treatment across both groups, regardless of clinical responses (Figures 2D and 2E; Figures S2B and S2C) or treatment arm (Figures S2D and S2E). Cycling cells, like epithelial cells, decreased upon treatment in both R and NRs. Cycling cells, which express high levels of cell cycle-related genes, form a distinct cluster. To reveal the cell type of the cells included in this cycling cluster, we performed label transfer analysis (Figure 2F; Figure S2F). Most cycling cells mapped to epithelial clusters (Figure 2F; Figure S2F), consistent with the proximity of these two clusters in the UMAP, with a small subset of 504 cycling T cells (Figure 2F).

Short-lived R ($n = 8$), who initially showed PR (week 8) but progressed by week 24, were categorized as NRs in the final evaluation at week 24. To assess differences between short-lived R, long-lived R (patients showing response at week 24), and NRs (no response at week 8), patients were grouped separately. Epithelial cell reduction upon treatment (week 3) was more significant in long-lived R compared to both short-lived R and NRs (Figure S2G). These findings suggest that distinct cell population dynamics correlate with treatment outcomes.

Myeloid cell states associated with response to chemoimmunotherapy

Myeloid cell fraction did not change upon treatment (Figure S2A). However, upon re-clustering of the myeloid cell compartment (Figure 3A), we observe distinct clusters of macrophage and monocyte cell populations differentially enriched in R vs. NR patients, prior to vs. upon treatment. We identified in total nine macrophage clusters, all highly expressing the tumor-associated macrophage marker *APOE*; three monocyte clusters, highly expressing the monocyte marker *S100A8*; one classic dendritic cell (DC) cluster, highly expressing *CD1C*; and one activated DC cluster, highly expressing *LAMP3* (Figure 3B; Figure S3B; Table S4). A cluster of cycling myeloid cells was also identified (Figure 3B; Figure S3B).

R patients display increased fractions of Mac_FOLR2 cells prior to treatment, and Mac_APOE cells on treatment, compared to NR patients (Figures 3C and 3D; Figure S3D). Both clusters consist of macrophages highly expressing markers such as *FOLR2*, *SELENOP*, *SLC40A1*, and *CCL18* (Figure S3B; Table S4) and show upregulation of a gene signature characteristic of tissue-resident FOLR2⁺ macrophages²⁹ (Figure S3C; Table S3). NR patients are mainly enriched in monocytes (Mono_S100A8) both prior to and upon treatment, compared to R (Figures 3C and 3D; Figure S3D). Mac_FOLR2 enrichment in R patients and Mono_S100A8 enrichment in NR patients were observed in both treatment arms, whereas Mac_APOE enrichment in R patients was more evident in R patients of arm A (Figure S3E).

Altogether, these results demonstrate that patients display enrichment in distinct myeloid subsets based on their response status.

Transcriptional states of CD3⁺ TILs in advanced TNBC

To investigate differential enrichment of T cell subsets based on response status, we re-clustered T cells independently of other TME cell types. Re-analysis of the 23,193 T cells, UMAP, and unsupervised clustering identified 12 distinct clusters, based on transcriptomes (Figures 4A and 4B). All clusters are represented across most samples, regardless of patient (Figures S4A and S4B) or tissue (Figure S4C) specificity. DE analysis and projection of T cell-specific gene signatures and markers (Figure 4C; Figure S4D; Table S3; Table S5) enabled annotation of these populations.

On the UMAP, CD4⁺ T cell clusters are located on the left and included 4 clusters: two expressing memory markers, e.g., *IL7R* (CD4_IL7R) and *SELL*, *LEF1*, and *TCF7* (CD4_LEF1), one cluster of conventional CD4⁺ cells (Tconv; CD4_CD40LG), and one cluster of regulatory T cells (Tregs_FOXP3). CD8⁺ T cell clusters were located on the right and included 4 clusters: one expressing classic cytotoxic/effector T cell markers, e.g., *FCGR3A*, *FGFBP2*, *PRF1*, and *GZMB* (CD8_GNLY), one expressing circulating/memory-precursor markers, e.g., *GZMK* and *KLRG1* (CD8_GZMK), one expressing memory-precursor markers and chemokine genes, e.g., *CCL4* and *CCL5* (CD8_CCL4), and one with marker of cytotoxicity, e.g., *GZMB*, dysfunction, e.g., *LAG3*, and tissue residency, e.g., *ITGAE*, as well as *CXCL13* (CD8_CXCL13) (Figure 4C; Figure S4D; Table S5). We also identified a natural killer cell cluster (CD8_TRDC) and 3 shared CD4⁺/CD8⁺ clusters: one expressing stress markers (such as ribosomal, mitochondrial, and heat-shock markers) (CD4/CD8_stress), one expressing interferon-associated genes (CD4/CD8_ISG15), and one expressing cell cycle genes (CD4/CD8_Cycling) (Figure 4C; Figure S4D; Table S5). Label transfer analysis of both the CD4/CD8_Cycling cluster and the T cell cycling subset of 504 cells, identified previously (Figure 2F), showed that most cycling cells are transcriptionally proximal to CD8_CXCL13 cluster (Figure 4D; Figure S4E).

Gene signature analysis revealed distinct dysfunctional states within CD8⁺ T cells. CD8_GZMK, CD8_CCL4, and CD8_CXCL13 clusters form a dysfunctional trajectory, while the CD8_GNLY cluster represents a terminal effector-memory state (Temra) (Figure 4E). Trajectory analysis using diffusion map pseudotime

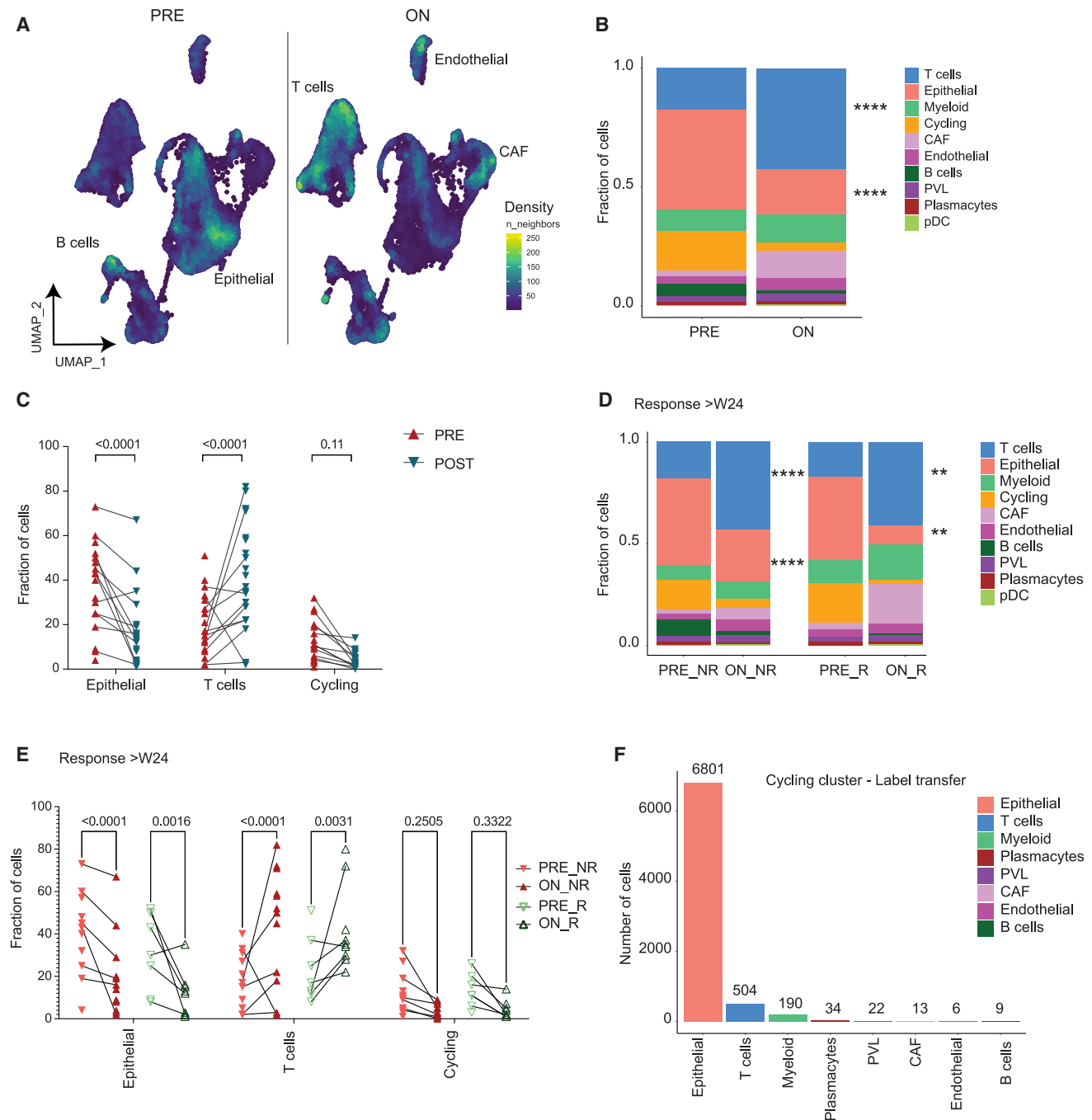


Figure 2. TNBC transcriptomic landscape dynamics at PRE- and ON-treatment states

(A) UMAP showing cell density split at PRE-treatment (week 0/baseline) and ON-treatment (week 3).

(B) Cluster frequency distribution at PRE- and ON-treatment (ordinary two-way ANOVA test, with Sidák correction for multiple comparisons; **** p value ≤ 0.0001).

(C) Fraction of epithelial cells (left), T cells (middle), and cycling cells (right) per sample at PRE- and ON-treatment (dots: biopsy samples; lines: paired samples; PRE: $n = 18$; ON: $n = 21$; exact p values shown; two-way ANOVA test, with Sidák correction for multiple comparisons; Progression_P19 sample collected at later time point was excluded from the analysis).

(D) Cluster frequency distribution comparing responders (R) and non-responders (NR) at PRE- and ON-treatment (PRE_NR: $n = 11$; PRE_R: $n = 7$; ON_NR: $n = 12$; ON_R: $n = 9$; ordinary two-way ANOVA, with Tukey correction for multiple comparisons; ** p value ≤ 0.01 , **** p value < 0.0001).

(E) Fraction of T cells (left), epithelial cells (middle), and cycling cells (right) comparing R and NR at PRE- and ON-treatment (same n as (D)); lines: paired samples; exact p values shown; ordinary two-way ANOVA test, with Tukey correction for multiple comparisons; Progression_P19 sample collected at later time point was excluded from the analysis).

(F) Distribution of cells label-transferred from the cycling cluster ($n = 7,579$) into the other clusters.

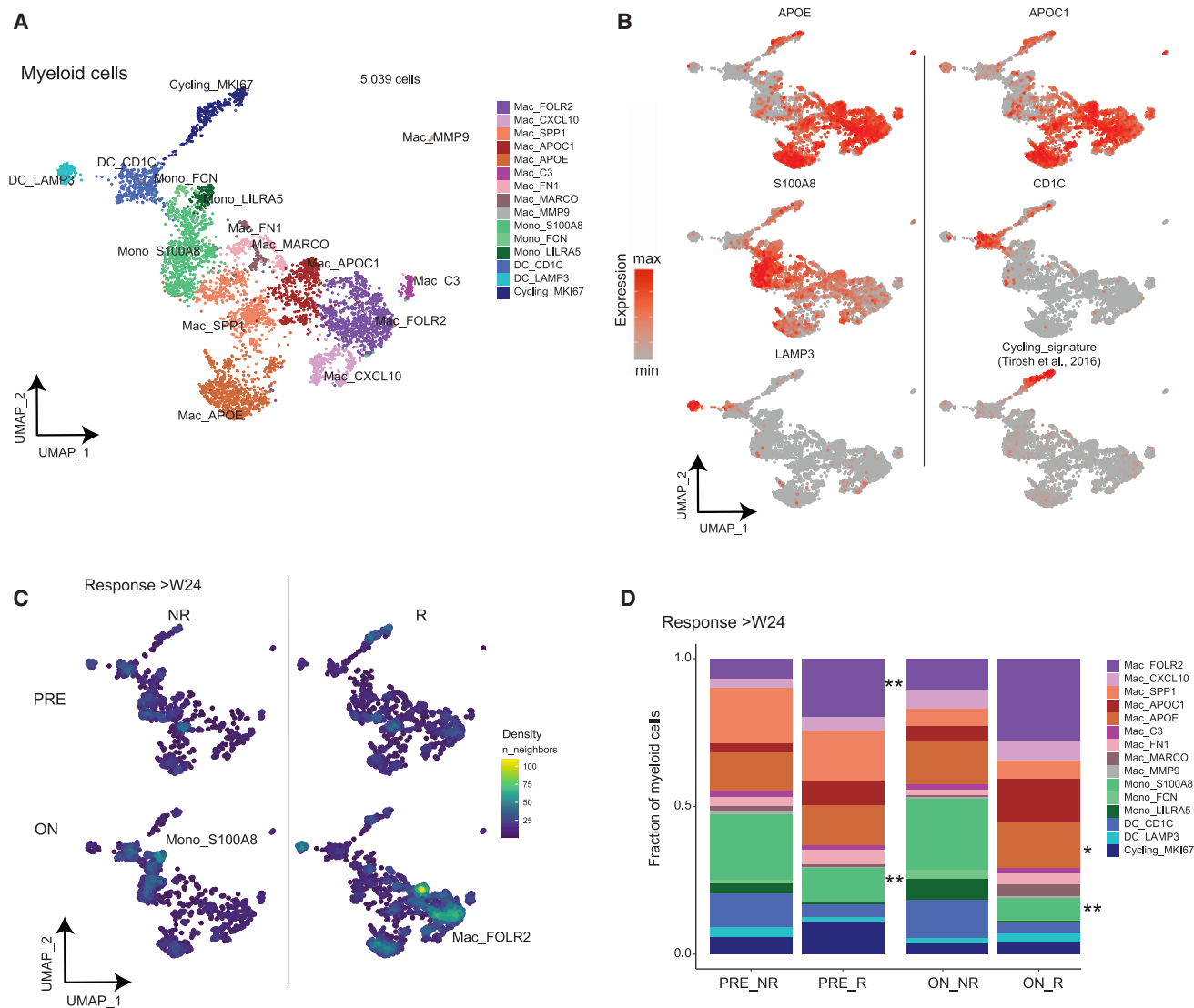


Figure 3. Myeloid cell cluster dynamics during chemoimmunotherapy

(A) UMAP of 5,039 tumor-infiltrating myeloid cells.

(B) Normalized expression of selected gene markers and signatures, demonstrating myeloid cell identities.

(C) UMAP showing myeloid cell density by biopsy time points (PRE- and ON-treatment) and response status at week 24.

(D) Myeloid cell cluster frequency distribution at PRE- and ON-treatment states comparing responders (R) and non-responders (NRs). (PRE_NR: $n = 7$; PRE_: $n = 4$; ON_NR: $n = 8$; ON_R: $n = 6$; Progression_P19 sample collected at later time point was excluded from the analysis; samples with <50 total myeloid cells were excluded from the analysis; ordinary two-way ANOVA, with Tukey correction for multiple comparisons; * p value ≤ 0.05 , ** p value ≤ 0.01).

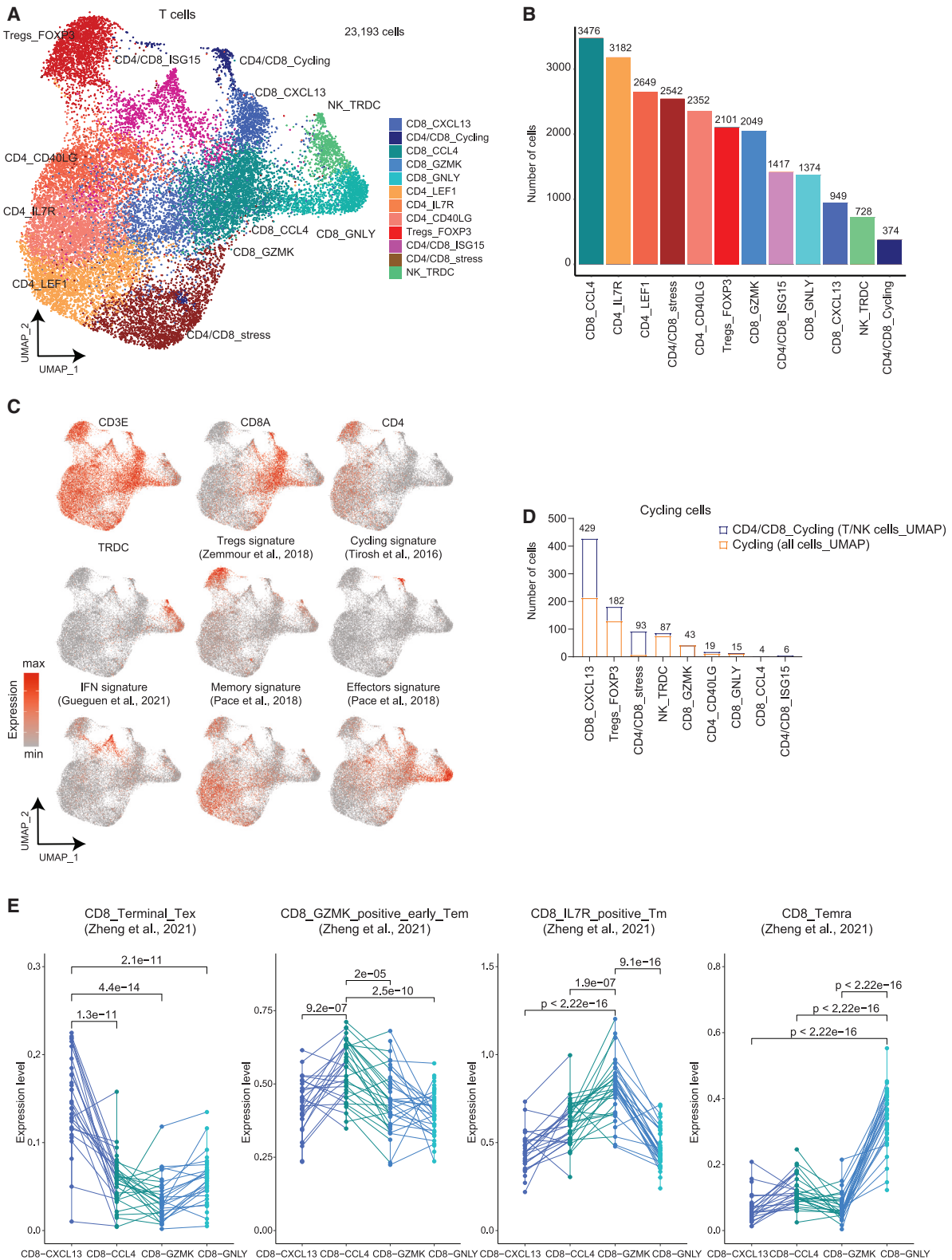
further validated these distinct paths, with terminal states of CD8_CXCL13 (terminal exhausted) and CD8_GNLY (Temra) (Figures S4F–S4H).³⁰ These results are consistent with the bifurcation CD8 T cell differentiation model described in the past on LCMV mouse study by Chen et al.³¹

Within the dysfunctional trajectory, we observe a continuum from early-dysfunctional/memory-precursor states CD8_GZMK and CD8_CCL4 to late-dysfunctional states CD8_CXCL13 (Figure 4E), with markers of dysfunction (e.g., *HAVCR2* and *LAG3*), tissue residency (e.g., *ITGAE*), cytotoxicity (e.g., *GZMB*), and increased proliferation. These results highlight the heterogeneity

of the CD8 TIL compartment, comprising early-dysfunctional memory-precursor states, terminally dysfunctional states, and terminal effector-memory states.

T cell states associated with response to chemoimmunotherapy

To identify T cell populations linked to clinical response, we analyzed cluster distributions across patients based on response status (R and NRs) and treatment time points (PRE- and ON-treatment). R display a significantly higher fraction of late-dysfunctional CD8_CXCL13 cells both PRE- and ON-treatment



(legend on next page)

(Figures 5A–5C; Figures S5A and S5B). Additionally, Tregs_{FOXP3} cells are expanded in R ON-treatment, particularly in patients receiving chemotherapy combined with aPD-L1 (arm B) (Figures 5C and 5G; Figures S5C and S5D). In contrast, NRs exhibit a higher fraction of CD8_{GNLy} Temra cells ON-treatment (Figures 5A–5C; Figures S5A and S5B).

Given the enrichment of CD8_{CXCL13} cells in R patients, both PRE- and ON-treatment, we further analyzed the expression of gene signatures associated with Temra or late-dysfunctional CD8⁺ T cell states.²¹ R patients show higher expression of late-dysfunctional gene signatures both PRE- and ON-treatment (Figure 5D, left panel). Conversely, NR patients upregulate Temra-associated gene signatures at both time points (Figure 5D, right panel). Consistent with these findings, DE analysis of CD8⁺ T cells between R and NR patients revealed that R upregulate genes associated with T cell exhaustion (such as *PDCD1*, *LAG3*, *TOX*, *HAVCR2*, and *RGS1*³²), at both time points (Figures 5E and 5F; Table S6). NR patients, instead, upregulate genes linked to conventional effector states (such as *FGFBP2*, *FCGR3A*, and *GNLY*) and memory genes (such as *TCF7*, *KLF2*, and *SELL*) (Figures 5E and 5F; Table S6).

These findings suggest that R are characterized by enrichment in late-dysfunctional CD8 T cells both PRE- and ON-treatment and Tregs ON-treatment, while NRs display higher levels of Temra CD8 T cells (Figures S5D and S5E).

The enrichment of CD8_{CXCL13} cells in R patients led to the hypothesis that these cells exhibit tumor-reactive properties. Supporting this, CD8_{CXCL13} cells displayed high expression of tumor-reactive gene signatures,³³ whereas CD8_{GZMK} memory-like progenitors and CD8_{GNLy} Temra cells upregulated viral-specific signatures,³³ indicative of bystander activity (Figure S5F).

Interestingly, some NR patients showed similar or even higher CD8_{CXCL13} fractions compared to R. Further stratification revealed that these were short-lived R, initially showing PR but later progressing (Figure S5G). Short-lived R exhibited an intermediate T cell profile, with high fractions of Temra CD8_{GNLy} cells both PRE- and ON-treatment (Figure S5G).

Next, to explore the potential synergistic effects between myeloid and T cells on response to chemoimmunotherapy, we performed correlation analysis of relative (sub)cluster abundancies in R patients, PRE-treatment (Figure 5H; left panel) and ON-treatment (Figure 5H; right panel). In R patients, PRE-treatment abundance of late-dysfunctional CD8_{CXCL13} cells and proliferating T cells correlated with enrichment in DC-CD1C and Mac-APOE macrophages. ON-treatment, Treg expansion correlated with Mac-FOLR2 and Mac-APOE macrophages, clusters associated with T cell infiltration and favorable antitumor

responses²⁹ (Figure 5H; Figure S3C). Additionally, ON-treatment, enrichment in pre-dysfunctional CD8_{CCL4} cells positively correlated with late-dysfunctional CD8_{CXCL13} cells (Figure 5H).

Altogether, these results suggest that high pre-treatment fractions of tissue-resident, late-dysfunctional CD8_{CXCL13} cells are associated with response to chemoimmunotherapy. In contrast, resistance is linked to increased levels of cytotoxic, non-dysfunctional CD8⁺ cells and memory CD4⁺ cells.

TCR clonal expansion patterns in R vs. NR patients with TNBC

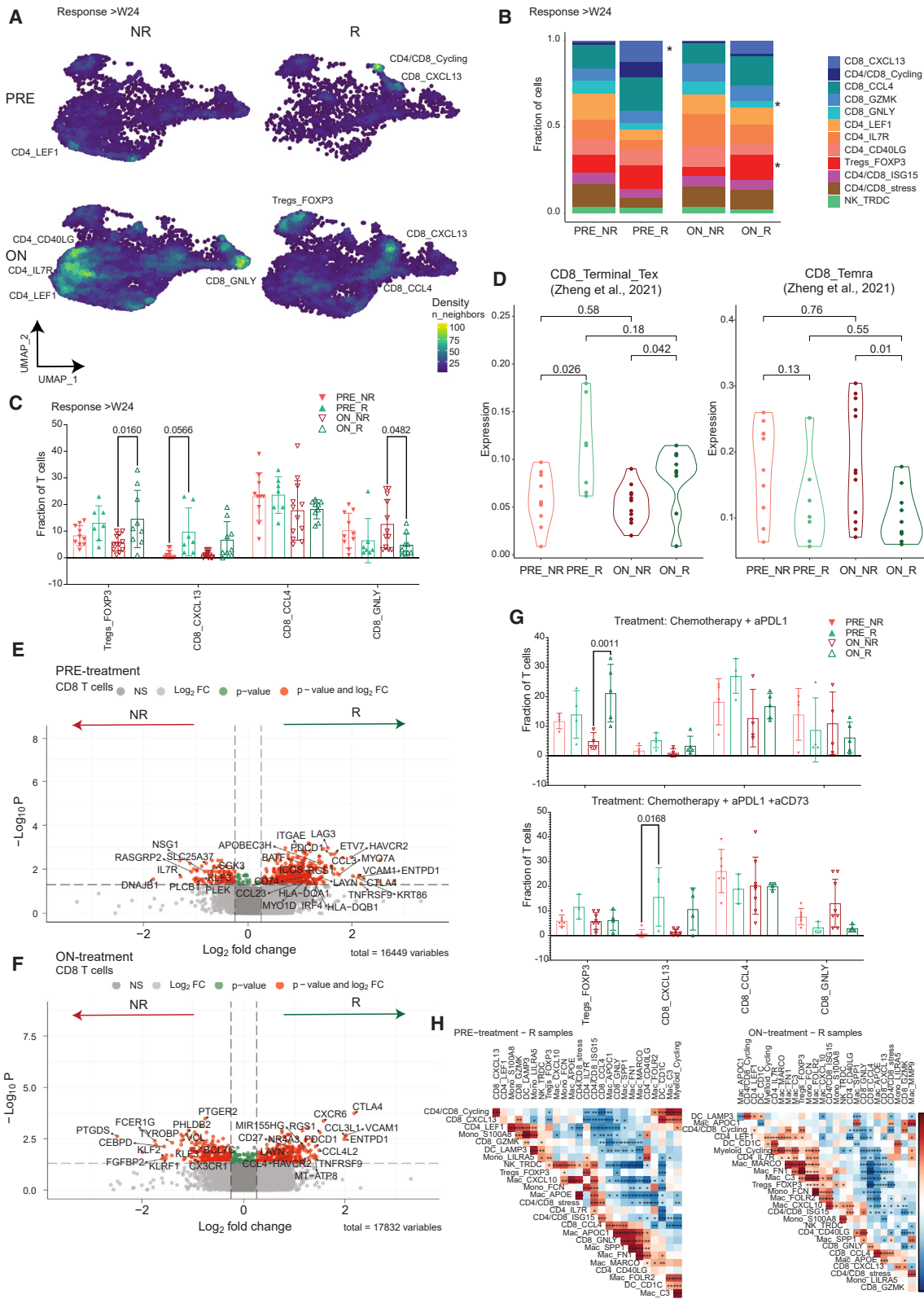
scTCR-seq with matched 5' RNA profiling was obtained for 36 out of 40 biopsies. We obtained total higher number of total cells with matched T cell receptor (TCR) and RNA profile in ON-treatment samples, compared to PRE-treatment, consistent with our findings on the increased T cell infiltration upon treatment, in all patients (Figure 6A) and in paired-sample patients alone (Figure S6A).

We first analyzed clonal expansion patterns in R vs. NR patients both PRE- and ON-treatment. R patients show higher clonal expansion PRE-treatment compared to NRs, quantified by the absolute number of cells and the relative abundance of highly expanded clonotypes (Figures 6A and 6B). Of note, across the different biopsies, we recovered different absolute cell numbers; thus, the clonal expansion pattern per patient and per response group state could be impacted by the cell size differences. To correct for this bias and equalize the relative contribution of the individual samples, we performed downsampling, with a total of $n = 78$ cells randomly selected per sample. This value was chosen based on sample size distribution, with procedure being repeated 100 times and results being averaged. We observe that the fraction of highly expanded clonotypes and mean clonotype size remained significantly higher in R than NR PRE-treatment (Figure 6C; Figure S6B).

Upon treatment, clonal expansion decreased in R, but not in NR patients (Figures 6C and 6D; Figure S6C). Our hypothesis is that this decrease in R was associated with reduced frequencies of the most expanded PRE-treatment clonotypes and the emergence of newly detected, lowly expanded clonotypes ON-treatment, in line with the observed increased T cell infiltration ON-treatment. To test this hypothesis, we focused our analysis on the paired samples. $n = 1$ out of the 12 paired patients was excluded from this analysis due to low cell number detected ON-treatment. We calculated the ratio of clonotypes detected only ON- and PRE-treatment (ON-only: PRE-only) (Figure 6E). R showed a significantly higher ON-only:PRE-only ratio for all clonotypes, including singletons, compared to NR patients

Figure 4. Characterization of T cell states in metastatic TNBC

- (A) UMAP of 23,193 tumor-infiltrating T cells, highlighting 11 T cell clusters and 1 NK cluster (NK: natural killer cells).
(B) Distribution of cell numbers across T cell clusters.
(C) Normalized expression of selected genes and gene signatures, defining T cell states.
(D) Distribution of T cells label-transferred from (1) the total T cell cycling cluster ($n = 504$ cells) and (2) the CD4/CD8_{Cycling} cluster ($n = 374$ cells) to the other T cell clusters.
(E) Mean expression of gene signatures, defining late-dysfunctional (CD8_{Terminal_Tex}), early effector-memory (CD8_{GZMK_positive_early_Tem}), IL7R memory (CD8_{IL7R_positive_Tm}), and terminal effector-memory (CD8_{Temra}) CD8 T cell states, in CD8⁺ T cells (including CD8_{CXCL13}, CD8_{CCL4}, CD8_{GZMK}, and CD8_{GNLy} clusters). Samples aggregated as pseudobulks; paired t tests, performed to compare mean signature expression across clusters (p values shown).



(legend on next page)

(Figure 6E, left panel). However, focusing on expanded clones (size ≥ 2 cells), NRs exhibited a higher ON-only:PRE-only ratio (Figure 6E, right panel).

To better illustrate this, we further compared clonotype frequencies in patients, PRE- and ON- treatment (Figures 6F and 6G). In R patients, PRE-treatment highly, expanded clones frequently persisted ON-treatment, though some declined in size or disappeared (Figures 6F and 6G, right panel). In NR patients, ON-treatment we observed newly emerging large, expanded clones, not existing prior to treatment (Figures 6F and 6G, left panel). This pattern, consistent across patients, suggests that baseline clonal expansion correlates with response. Upon treatment, R display an influx of new, lowly expanded clonotypes alongside retained clones.

To explore clonal sharing as an indicator of clonal reinvigoration, we analyzed paired biopsies. When including all clonotypes, we observed a higher fraction of shared clonotypes in R, compared to NR patients (Figure S6D), whereas clonal sharing index (Jaccard) tended to be higher in R patients (Figures S6E and S6F). For some biopsies, however, the number of retrieved T cells was relatively small, so we examined how sensitive the clonal sharing index is to the sample size. To do so, we performed an *in silico* downsampling experiment. Firstly, we randomly selected an equal number of cells from varying sample sizes, and next we calculated the clonal sharing indices (Jaccard and Morisita) between PRE- and ON-treatment time points. We observed that the values of both clonal sharing indices tend to decrease as the sample cell number decreases (Figure S6G), indicating that clonal sharing indices are influenced by sample size. Therefore, we cannot conclude with confidence about the differences in the total clonal sharing status between PRE- and ON-treatment states. Additionally, we examined clonal sharing between the top 10% most expanded clonotypes PRE- and ON-treatment per patient (Figure S6H). In R, many top expanded PRE-treatment clonotypes remained among the most expanded ON-treatment, whereas in NRs, top expanded PRE-treatment clonotypes were generally not retained ON-treatment (Figure S6H). One exception was patient P10, a short-lived R who initially exhibited PR but later progressed.

Taken together, these results indicate that increased clonal expansion PRE-treatment is associated with response to che-

moimmunotherapy. R exhibit reduced clonal expansion, driven by the decline of highly expanded clones and the recruitment of new clonotypes. This is indicative of an ongoing clonal replacement by newly recruited T cell clones that have probably recently entered the tumor site and have not yet fully expanded.

Distinct clonal expansion distribution per T cell cluster between R and NR patients with TNBC

We next mapped the TCR profiles to the T cell UMAP reference to examine TCR clonal patterns across different T cell clusters in R vs. NR patients. Among all T cell populations, CD8_CXCL13 cells exhibit higher clonal expansion levels (Figures 7A and 7B; Figure S7A). Notably, expansions in the CD8_CXCL13 cluster occur almost exclusively in R, but not in NR patients, both PRE- and ON-treatment (Figure 7C), a trend consistent across patients (Figure 7D). Large clonal expansions are also observed in the CD4/CD8_Cycling cluster (Figures 7B and 7C), which mainly contains proliferating CD8_CXCL13 cells (Figure 4D; Figure S4E). TCR analysis confirms strong clonal sharing between CD4/CD8_Cycling and CD8_CXCL13 populations (Figures S7B and S7C).

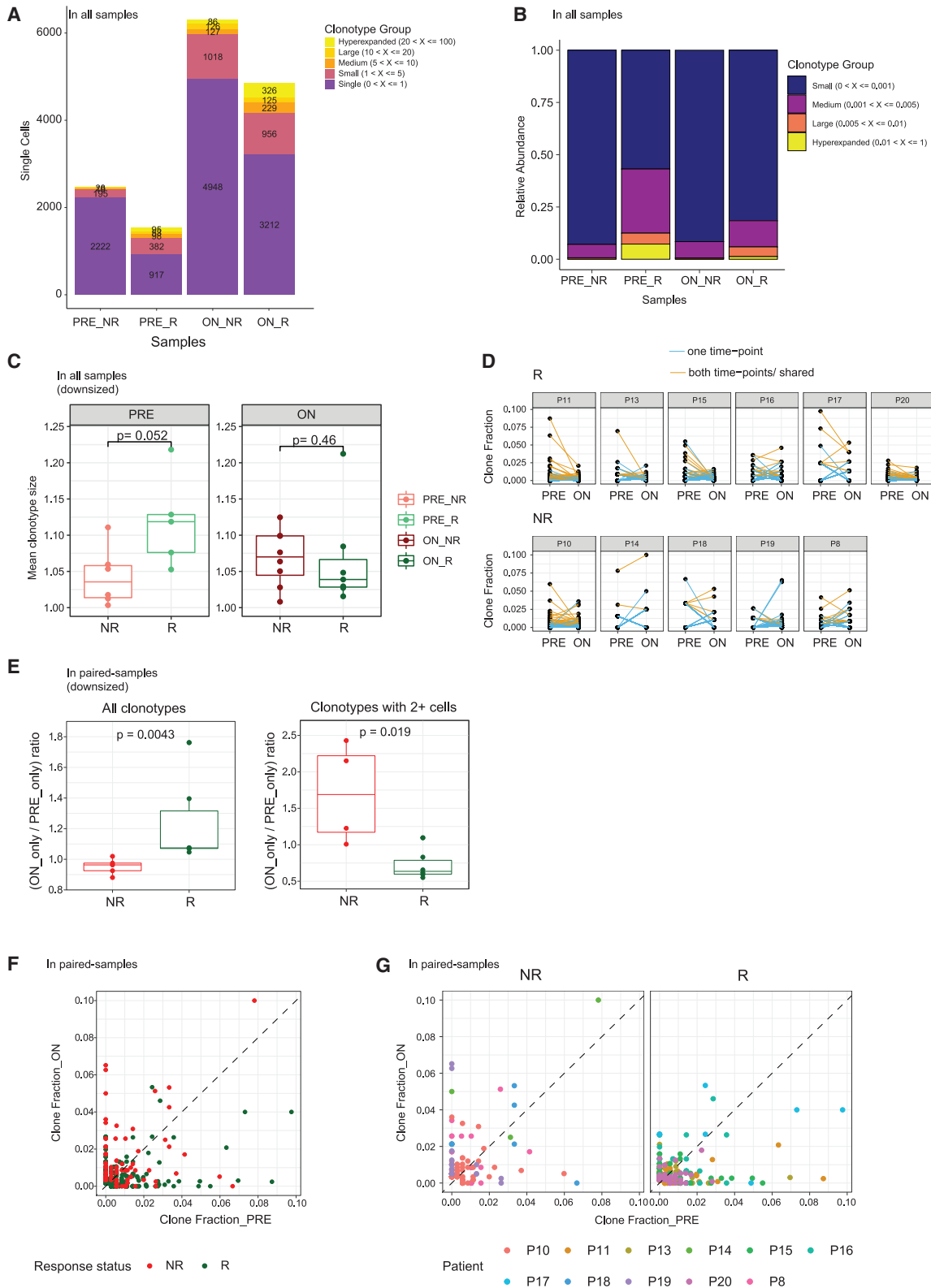
Early-dysfunctional (memory-precursor) CD8_CCL4 cells are significantly clonally expanded prior to treatment in both R and NR patients (Figures 7C and 7D). In general, these cells can act as a source that gives rise to late-dysfunctional (CD8_CXCL13) cells, helping sustain T cell responses over time.²² Interestingly, upon treatment, CD8_CCL4 expansion increases in R but not in NR patients (Figure 7D). Conversely, NR patients show significant clonal expansions in the CD8_GNLY Temra cluster upon treatment (Figure 7D).

Together, these results indicate that R patients display expansions in late-dysfunctional CD8_CXCL13 cells, both prior to and upon treatment. Additionally, there is an increased clonal expansion in the CD8_CCL4 precursors of late-dysfunctional cells in R patients, while NR patients show expansions in the CD8_GNLY cluster, characterized by effector but not dysfunctional genes. These findings highlight the importance of clonal expansions across the dysfunctional axis, from early- to late-dysfunctional clusters, for sustained antitumor responses.

We next analyzed shared clonotypes detected in both PRE- and ON-treatment time points for $n = 11$ patients with paired

Figure 5. Identification of T cell populations associated with response to treatment

- (A) UMAP showing cell density at PRE- and ON-treatment states, comparing responders (R) and non-responders (NRs) based on the RECIST criteria (week 24).
 (B) Distribution of T cell frequencies at PRE- and ON-treatment states for R and NR (two-way ANOVA; * p value ≤ 0.05).
 (C) Fraction of T cell clusters per sample at PRE- and ON-treatment for R and NR (dots: biopsy samples; PRE_NR: $n = 10$; PRE_R: $n = 7$; ON_NR: $n = 12$; ON_R: $n = 9$; Progression_P19 sample collected at later time point was excluded from the analysis; Baseline_P26 biopsy was excluded due to low cell count; exact p values by ordinary two-way ANOVA test, with Tukey correction for multiple comparisons; non-represented p value = ns).
 (D) Normalized expression of selected gene signatures, defining late-dysfunctional (left) and terminal effector-memory CD8⁺ T cell states (right) comparing R and NR at PRE- and ON-treatment. Analysis performed on CD8⁺ T cells (CD8_CXCL13, CD8_CCL4, CD8_GZMK, CD8_GNLY clusters). Samples aggregated as pseudobulks; t tests performed to compare mean gene signature expression across patient groups (p values shown).
 (E and F) Volcano plots of differentially expressed genes in CD8⁺ T cells between R and NR patients at PRE-treatment (E) and ON-treatment (F). Red dots indicate genes with adj. p value < 0.05 and fold change > 0.25 . Samples aggregated as pseudobulks.
 (G) Upper: T cell cluster fractions for R and NR at PRE- and ON- treatment in arm B (chemotherapy + aPD-L1; $N = 12$ patients, including $N = 6$ with paired samples: $N = 2$ NR and $N = 4$ R; PRE_NR: $n = 4$; PRE_R: $n = 4$; ON_NR: $n = 4$; ON_R: $n = 5$). Lower: T cell fractions in arm A (chemotherapy + aPD-L1 + aCD73; $N = 15$, including $N = 6$ with paired samples: $N = 4$ NR and $N = 2$ R; PRE_NR: $n = 6$; PRE_R: $n = 3$; ON_NR: $n = 8$; ON_R: $n = 4$). Dots represent biopsy samples; exact p values shown, ordinary two-way ANOVA test, with Tukey correction for multiple comparisons; non-represented p value = ns. Progression_P19 sample collected at later time point was excluded from the analysis; Baseline_P26 biopsy was excluded due to low cell count.
 (H) Pearson correlation of myeloid and T cell cluster abundancies in R patients at PRE- (left) and ON- (right) treatment states (* p value ≤ 0.05 , ** p value ≤ 0.01 , *** p value ≤ 0.001).



(legend on next page)

samples. We observed that at baseline, shared clonotypes have distinct T cell cluster distribution profiles between R and NR patients. In PRE-treatment samples, shared clones in R patients are mainly found in dysfunctional CD8_CXCL13 and in CD4/CD8_Cycling clusters (that, as described before, are for the vast majority CD8_CXCL13 cells); whereas, in NR patients, they are mainly present in memory-precursor CD8_CCL4 and in Temra CD8_GNLY clusters (Figure 7E; Figure S7D). Analysis of the expansions of shared clones PRE- vs. ON-treatment unveils that, ON-treatment, there is a decreased fraction of CD8_CXCL13 and an increased fraction of memory-precursor CD8_CCL4 cells in R patients (Figures 7E and 7F). NR patients, upon treatment, exhibit a significant decrease in the fraction of the memory-precursor CD8_CCL4 cells, in contrast to the R group (Figures 7E and 7F). On the other hand, in NR patients, upon treatment, we observed increased clonal expansions within the Temra CD8_GNLY cluster. Altogether, these results suggest that both a high fraction of CD8_CXCL13 cells PRE- and ON-treatment and a continuous replenishment of the memory-precursor pool are associated with an objective response to chemoimmunotherapy.

We further examined the distribution of non-shared T cell clones found either PRE- or ON-treatment only (Figures S7E–S7H). In R patients, newly emerging clones are mainly found in CD8_CXCL13 and CD8_CCL4 clusters, as well as in CD4⁺ T cell clusters, including CD4/CD8_ISG15, conventional T cells (CD4_CD40LG), and Tregs (Tregs_FOXP3) (Figures S7E and S7F). In contrast, in NR patients, expanded clonotypes are predominantly found in memory CD4⁺ T cell clusters (CD4_LEF1 and CD4_IL7R) and the CD8_GNLY Temra cluster, with minimal representation in CD8_CXCL13 (Figures S7E–S7G).

Overall, these results highlight the clonal diversification of the TCR repertoire in R vs. NR patients, with R showing higher expansions in late-differentiated CD8⁺ T cells co-expressing markers of both dysfunction and activation (CD8_CXCL13).

DISCUSSION

In the current study, we examined the temporal dynamics of TILs in patients with metastatic TNBC treated with chemoimmunotherapy in a phase 2 clinical trial. Patients were randomized to

two treatment arms to assess the benefit of adding aCD73/oleclumab to chemotherapy plus aPD-L1/durvalumab. Notably, patients were randomized to the either of these arms irrespective of PD-L1 or CD73 expression. In previous studies (IMpassion130, KEYNOTE 355), adding PD-L1 blockade (atezolizumab and pembrolizumab, respectively) to chemotherapy showed significant progression-free survival benefit in patients with PD-L1-positive advanced TNBC, compared with chemotherapy alone.^{34,35} However, the IMPASSION-131 trial did not report any benefit in patients who received atezolizumab treatment in addition to chemotherapy alone.³⁶ The SYNERGY trial was designed before the notion of benefit of PD-L1 blockade in PD-L1-positive, metastatic TNBC tumors; thus, it did not enrich for such subset. Although, the addition of oleclumab to durvalumab plus chemotherapy was not associated with improved clinical benefit at week 24,³⁷ we sought to investigate the anti-tumor immune response prior to and during treatment to identify differential features linked to clinical outcomes.

Prior to treatment, we observed that R have a significantly higher fraction of clonally expanded CD8⁺ T cells, with increased expression of genes associated with T cell dysfunction, cytotoxicity, and tumor reactivity. Upon treatment, a large influx of new clonotypes emerges in R patients, which likely represent recently infiltrated clonotypes that are thus not yet fully expanded. The higher proportion of late-dysfunctional CD8_CXCL13 cells in R patients was correlated with an increased frequency of macrophages expressing FOLR2, a macrophage subset recently associated with greater CD8⁺ T cell infiltration, and improved outcomes in BC.²⁹ Additionally, R patients showed an expansion of precursor CD8⁺ T cells (CD8_CCL4) upon treatment. In contrast, NRs exhibited a less diversified T cell repertoire, with expansions primarily observed in memory CD4⁺ T cell clusters and the CD8_GNLY Temra cells.

Altogether, these findings indicate that, maintaining a protective antitumor immune response requires a higher fraction of late-dysfunctional CD8⁺ T cells (CD8_CXCL13), likely endowed with superior functionality, along with an expansion of the memory-precursor CD8⁺ T cell pool to continuously replenish the CD8_CXCL13 subset.

CD39 and CD73 catalyze the conversion of ATP to AMP and AMP to ADO, respectively. Adenosine binds to A2a and A2b

Figure 6. TCR repertoire profiles of R and NR patients

(A) Quantification of clonal size across R and NR patients at PRE- and ON-treatment states. Clonotypes are ranked by expansion level: single (1 cell), small (>1 and <5 cells), medium (>5 and <10 cells), large (>10 and <20 cells), and hyperexpanded (>20 and <100 cells). The bars represent the number of cells belonging to each clonotype rank; *n* = 36 biopsy samples included.

(B) Relative clonal abundancies R and NR patients at PRE- and ON-treatment states; *n* = 36 biopsy samples included.

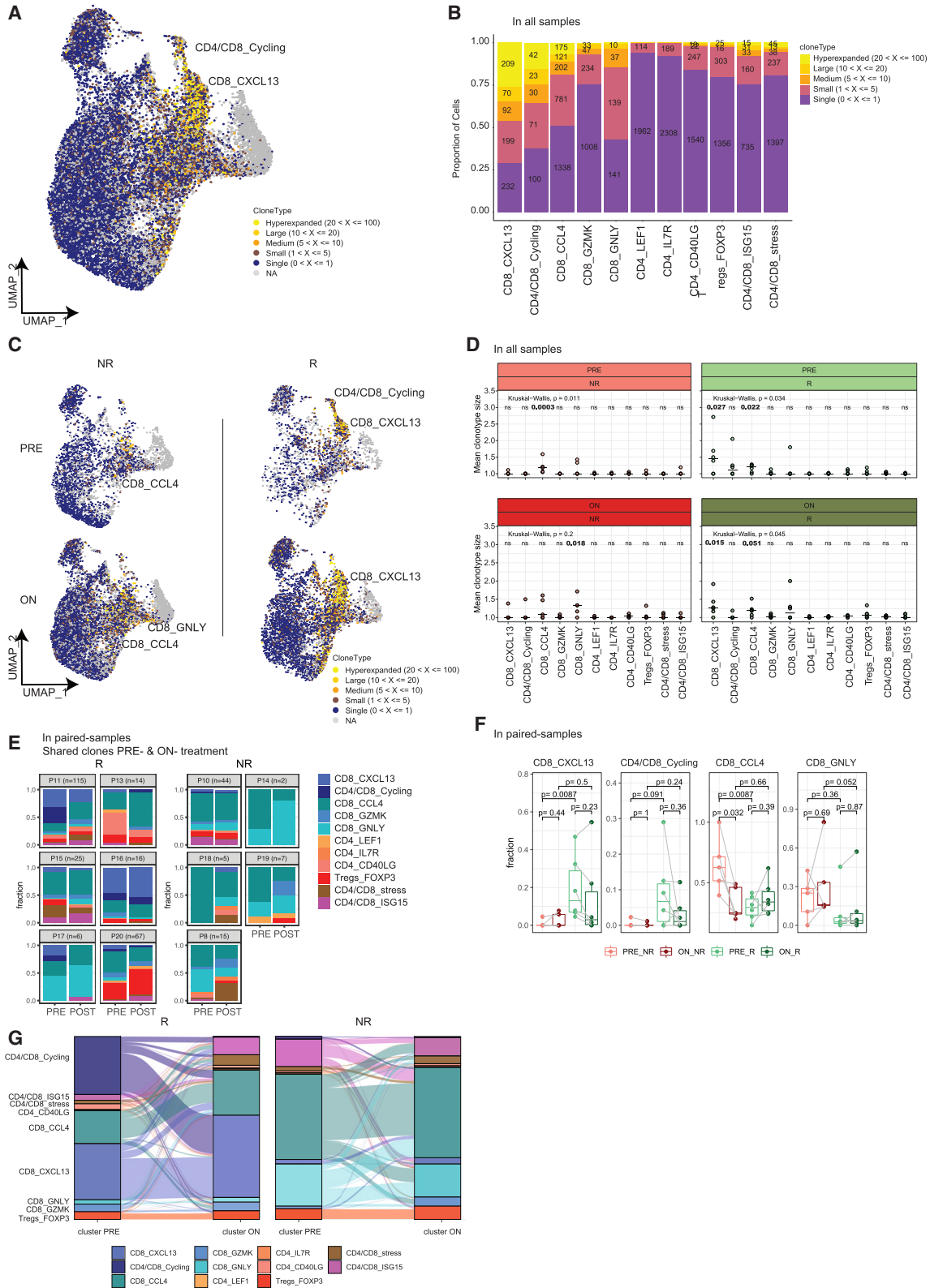
(C) Mean clonal expansion levels in R and NR patients at PRE- and ON-treatment states. Each dot represents the mean clonotype size per patient at a given time point, based on downsized samples (78 cells per sample; see Methods for details). Wilcoxon test *p* values indicate statistical significance.

(D) Clonotype frequency dynamics from PRE-to ON-treatment, shown per patient. Each dot represents a clonotype's frequency at a given time point, with lines connecting frequencies of the same clonotype. Lines are orange if the clonotype is present at both time points and blue if unique to one time point. Upper: R patients (*n* = 6); lower: NR patients (*n* = 5).

(E) Ratios of clonotypes detected only at ON- vs. PRE-treatment (ON-only:PRE-only). Left: all clonotypes (including singletons); right: expanded clonotypes (≥2 cells). Analysis includes *n* = 11 paired patients (6 R, 5 NRs), with downsizing to 78 cells per sample. Wilcoxon *p* values are shown. Patients with same ratio value are represented in the same point.

(F) Scatterplot comparing TCRβ clonotype frequencies at PRE- (*x* axis) and ON-treatment (*y* axis) in all paired PRE- and ON-treatment samples (*n* = 11 patients). Points represent clonotypes, color-coded by response status (R: *n* = 6, NRs: *n* = 5).

(G) Scatterplots showing TCRβ clonotype frequency comparisons (PRE-treatment: *x* axis; ON-treatment: *y* axis) for paired samples, color-coded by patient identity. Left: R patients (*n* = 6); right: NR patients (*n* = 5). Each point corresponds to one clonotype.



(legend on next page)

receptors on T cells, dampening TCR signaling and impairing T cell effector functions.^{38,39} The mechanisms underlying the correlation between CD73 blockade and response to treatment remain unclear. In our study, we observed a higher fraction of Tregs in R patients receiving chemotherapy with aPD-L1 alone. Since Tregs largely express CD73,⁴⁰ the addition of oleclumab could affect their function. While Tregs are associated with immunosuppressive phenotypes⁴¹ and poor responses to ICB, their abundance in R patients might reflect control of an active anti-tumor immune response, absent in NR patients. Thus, better understanding of Treg intratumoral heterogeneity and the role of each subset in antitumor immunity is essential.

Several studies highlighted that T cell infiltration correlates with favorable prognosis and OS in human tumors.⁴² Here, we observed that higher T cell clonal expansion prior to treatment is associated with response to chemoimmunotherapy. However, upon treatment, overall T cell expansion is similar in R and NR patients, with higher proportions of T cells compared to pre-treatment biopsies. Previous studies indicate that memory-precursor T cell subsets expand upon ICB treatment,^{22,23,43–45} while more recent research highlights the role of tumor-reactive, tissue-resident CD8⁺ T cell subsets, exhibiting exhaustion and activation markers associated with improved prognosis.^{24,46–48} Our findings align with this literature, with CD8_CXCL13 being the primary expanded subset in R patients. CXCL13 is a B cell chemoattractant that promotes the formation of tertiary lymphoid structures (TLSs) in tumors.⁴⁹ TLSs are involved in initiating and maintaining T cell and B cell responses in tumors, and their presence is linked with favorable clinical outcomes.⁵⁰ Recent studies suggest that CXCL13 expression by CD8⁺ T cells, along with other markers such as *ITGAE/CD103* and *ENTPD1/CD39*,⁴⁶ is indicative of tumor-reactive T cells.^{51,52} Further studies are needed to clarify the exact role of CXCL13⁺ CD8⁺ T cells in TLS formation and their impact on antitumor responses.

TCR sequencing analysis revealed that, before treatment, R patients have significantly higher clonal expansion levels compared to NR patients, suggesting that TCR expansion could predict responses to ICB. Upon treatment, R patients showed a decrease in mean clonotype size, which is due to two factors: (1) a significant decrease in the fraction of PRE-

treatment highly expanded clonotypes, primarily exhausted CD8_CXCL13 cells, and (2) an influx of newly emerging small clonotypes ON-treatment. In R patients, but not NR patients, expansions were observed within the CD8_CXCL13 cluster both prior to and during treatment, with highly expanded clones at baseline found again during treatment. These results suggest that most clonotypes expanded in R patients during treatment were already present before treatment. A recent study in basal and squamous cell carcinoma found that clonotypes expanded after PD1 blockade were not detectable before treatment,⁵³ indicating clonal replacement of tumor-reactive T cells. This discrepancy may be due to differences in TCR sequencing kinetics and earlier tissue sampling in our study (week 3 on-treatment) compared to the study by Yost et al.⁵⁴ (week 9 on-treatment).

Based on our results, we propose that both clonal reinvigoration of highly expanded pre-existing clones, together with clonal replacement ON-treatment, occur in patients that respond efficiently to chemoimmunotherapy treatment. Together, these findings suggest an immediate clonal expansion upon ICB treatment, followed by a rise of new clonotypes at later time points, through clonal replacement and recruitment from the periphery.

In NR patients, instead, we observe a higher fraction and expansion of CD8_GNLY Temra cells, which appear to be non-tumor-reactive bystanders, potentially recognizing viral antigens.⁵⁵ Bystander T cells generally lack chronic exhaustion features and resemble memory or effector memory T cells. Since exhaustion is driven by continuous antigen presentation,⁵⁶ T cells without tumor specificity are unlikely to undergo exhaustion. A recent study in melanoma demonstrated that TILs with cancer-recognizing TCRs exhibit exhaustion features, while T cells recognizing Epstein-Barr virus antigens form non-exhausted clusters.³³ To predict the specificity of these T cells, computational approaches are being developed,⁵⁷ based either on machine learning (e.g., TCRex⁵⁸ and NetTCR⁵⁹) or on sequence similarity clustering (e.g., GLIPH⁶⁰ and TCRdist⁶¹) that utilize the assumption that TCRs with the same antigen specificity should share some sequence motif. Future studies will help refine our understanding of TCR specificity and contribute to the development of more effective immunotherapeutic strategies.

Figure 7. TCR clonal dynamics between T cell clusters in R and NR patients

- (A) UMAP of T cell clonal size. Clonotypes are ranked by expansion level: single (1 cell), small (>1 and <5 cells), medium (>5 and <10 cells), large (>10 and <20 cells), and hyperexpanded (>20 and <100 cells); $n = 36$ biopsy samples are included in the analysis.
- (B) Quantification of clonal size per T cell cluster. Clonotypes are ranked by expansion level, as in (A); $n = 36$ biopsy samples are included in the analysis.
- (C) UMAP of T cell clonal size per patient group, displaying PRE- and ON-treatment states in R and NR patients.
- (D) Quantification of TCR expansion per T cell cluster at PRE-treatment (upper) and ON-treatment (lower) time points, separated by response status. Each point represents the mean clonotype size computed for T cells in each cluster for a given patient. Wilcoxon tests were performed to compare the mean clonotype size between a given cluster and the rest; significant p values are shown. Kruskal-Wallis tests were used to assess variability across clusters.
- (E) Distribution of cluster identities for clonotypes shared between PRE- and ON-treatment time points. Left: R patients; right: NR patients. Clonal size is indicated on top of the bar plot.
- (F) Dynamics of the fraction occupied by cells with selected cluster identity at PRE- and ON-treatment. Only clonotypes shared between PRE- and ON-treatment time points are considered (same data as in E). Each point represents the fraction of cells with a given cluster identity in a single patient. Points corresponding to the same patient are connected with a line (R patients: $n = 6$; NR patients: $n = 5$). Unpaired Wilcoxon test was performed for comparisons between PRE_NR vs. PRE_R and ON_NR vs. ON_R. Paired Wilcoxon test was performed for comparisons between PRE_NR vs. ON_NR and PRE_R vs. ON_R. Exact p values are shown.
- (G) Alluvial plot depicting cluster distribution for shared clonotypes between PRE- and ON-treatment time points in R (left) and NR (right) patients. Lines connect identical clonotypes shared between the two states.

Limitations of the study

Our study explored T cell transcriptomic and TCR dynamics in metastatic TNBC during chemoimmunotherapy, identifying subpopulations and TCR patterns associated with treatment response. We acknowledge that the limited sample size restricts the generalizability of our findings and prevents drawing conclusions about differences between treatment arms, including the potential impact of oleclumab addition. Additionally, the absence of certain TCR clones in pre-treatment samples, but their detection post treatment, could be attributed to sampling limitations rather than true clonal absence, a common challenge in TCR sequencing studies. Finally, while we identified immune subsets and clonal expansions linked to response, the underlying mechanisms remain unclear, warranting larger studies and functional analyses to validate and refine these findings.

RESOURCE AVAILABILITY

Lead contact

Further information and requests should be directed to and will be fulfilled by the lead contact, Dr. Emanuela Romano (emanuela.romano@curie.fr).

Materials availability

This study did not generate any new materials.

Data and code availability

- Single-cell omics data (including scRNA-seq and scTCR-seq) are publicly available in European Genome-Phenome Archive (EGA) in filtered count matrix format, under the database accession number: EGAD5000000748.
- The data are available under restricted access after review by the Data Access Committee (DAC) because these are human data generated from medical research. Individual, de-identified, participant read count and clinical data will be accessible for research purposes only as specified in the data access policy. After review of the request, the data access decision will be passed to the EGA database within four weeks, and an access account will then be granted. In case of publication(s) from the requester, the data will be available for 2 years from the date of last publication.
- This paper does not report original code. All custom code used for the analysis was written with existing software as detailed in the [STAR Methods](#) section and is available upon request.
- Any additional information required to reanalyze the data reported in this work paper is available from the [lead contact](#) upon request.

ACKNOWLEDGMENTS

C.M. received PhD fellowships from International Research Institute Servier, INCEPTION program (Institut Convergence, supported by Investissement Avenir), and funds by the PhD Program "FIRE - Program Bettencourt." V.L. was supported by a scholarship from The Belt and Road Master Fellowship program. E.T. was supported by a postdoctoral fellowship abroad from the AIRC (2018/2020-54 number: 20934). D. Lambrechts is supported by Research Foundation Flanders (FWO) (G0B6120N, G093821N), Stichting Tegen Kanker (C/2020/1529), Grand Challenges Program of VIB, European Union's Horizon 2020 Research, Innovation Programme (grant agreement no. 847912; RESCUE), KU Leuven internal fund (C14/18/092 and C14/22/125), and ERC fund (EXPAND IT - 101055422). S.A. received funding from the Institut Curie, Institut National de la Santé et de la Recherche Médicale, and Centre National de la Recherche Scientifique. E.R. was supported by CIC IGR-Curie 1428, ANR-10-IDEX-0001-02 PSL, and ANR-11-LABX-53 0043, Fondation ARC (grant no. AAP SIGN'IT 2019), Institut National Du Cancer PRT-K22-117.

High-throughput sequencing was performed by the ICGex NGS platform of the Institut Curie and by VSC (Flemish SuperComputer Center). The computational resources and services for demultiplexing and aligning the samples were performed by the Bioinformatics platform of the Institut Curie and by VSC. ICGex NGS platform of the Institut Curie is supported by the grants ANR-10-EQPX-03 (Equipex) and ANR-10-INBS-09-08 (France Génomique Consortium) from the Agence Nationale de la Recherche ("Investissements d'Avenir" program), by the ITMO-Cancer Aviesan (Plan Cancer III), and by the SiRIC-Curie program (SiRIC Grant INCa-DGOS-465 and INCa-DGOSInserm_12554). VSC is funded by the Research Foundation Flanders (FWO) and the Flemish Government – department EW1.

We thank C. Goudot for helpful discussions. We thank C. Martinat for support with samples provision. We thank the Association Jules Bordet for financial support with samples sequencing. We thank all the clinical teams of Institut Curie, Institut Bordet, and University Hospital Leuven, as well as all patients and their families.

AUTHOR CONTRIBUTIONS

C.M. performed experiments, curated the data, analyzed and interpreted scRNA/TCR-seq data, and wrote the original draft; V.K. analyzed and interpreted scTCR-seq data; B.B. curated the data; E.T. provided expertise and interpreted scRNA-seq data; P.-E.B. provided expertise on scRNA-seq data analysis; L.W. and X.W. performed experiments; M.E. and B.A. provided critical reagents and software; D. Loirat, P.A., K.P., H.W., L.B., and E.R. included, treated the patients in the clinical trial, and provided patient tissue samples; C.S. supervised scRNA-seq; J.J.W. provided expertise on scRNA-seq/TCR-seq analysis; T.M., A.W., O.L., and S.A. interpreted and supervised scTCR-seq analyses; L.B. conceived the clinical trial and the tissue sample collection; and D. Lambrechts, S.A., and E.R. supervised jointly the work, interpreted the data, provided fundings, and wrote the original draft. All co-authors edited the original draft and approved the manuscript.

DECLARATION OF INTERESTS

This study is supported by AstraZeneca, and drug supply for oleclumab and durvalumab is provided by AstraZeneca. This work has received support under the program France 2030 launched by the French Government. E.R. reports funding to her institution from Bristol Myers Squibb (BMS), AstraZeneca, Janssen-Cilag, Replimmune, and from Fonds Amgen France pour la Science et l'Humain and travel support from BMS, Hoffmann La Roche, AstraZeneca, and Merck Sharp & Dohme. S.A. is a shareholder and consultant for Mmemo Therapeutics. L.B. is supported by the Belgian "Fondation Contre le Cancer" and reports funding to her institution from AstraZeneca and travel support from Gilead. P.A. reports speaker fees and honoraria for consultancy and advisory board functions from Boehringer Ingelheim, Macrogenics, Roche, Novartis, Amcure, Servier, G1 Therapeutics, Radius, Deloitte, Synthon, Amgen, Novartis, and Gilead, travel grants from Amgen, MSD, Pfizer, Roche, and Daiichi Sankyo, and research funding from Roche. K.P. reports research grants to institute from MSD and Sanofi, speaker fees and honoraria for consultancy and advisory board functions from Astra Zeneca, Eli Lilly, Exact Sciences, Focus Patient, Gilead, MSD, Novartis, Pfizer, Roche, and Seagen, speaker fees and honoraria for consultancy and advisory board functions to institution from AstraZeneca, Eli Lilly, Exact Sciences, Gilead, MSD, Novartis, Pfizer, Roche, and Seagen, stock options from Need Inc., and travel grants from Astra Zeneca, Novartis, Pfizer, PharmaMar, and Roche. M.P.-G. reports financial interests, personal, invited speaker: AstraZeneca, Lilly, MSD, Novartis, and Pfizer; financial interests, personal, other, consultant: Camel-IDS/Precirix; financial interests, personal, advisory board: Immunomedics, Menarini, Odonate, Seattle Genetics, Immuteq, Seagen, Gilead, NBE Therapeutics, and Frame Therapeutics; financial interests, personal, advisory board, consultant, and invited speaker: Roche-Genentech; financial interests, personal, invited speaker, scientific board: Oncolytics; financial interests, institutional, research grant: AstraZeneca, Immunomedics, and Lilly; financial interests, institutional, funding: Menarini, MSD, Novartis, Pfizer, Radius, Roche-Genentech, Servier, and Synthon.

STAR★METHODS

Detailed methods are provided in the online version of this paper and include the following:

- **KEY RESOURCES TABLE**
- **EXPERIMENTAL MODEL AND STUDY PARTICIPANT DETAILS**
 - Study design
 - Human specimens
- **METHOD DETAILS**
 - Biopsy tissue dissociation
 - Red blood cell and dead cell removal
 - Sc-RNA-seq and TCR-seq profiling
 - scRNA data processing
 - Principal component analysis (PCA), UMAP clustering & downstream analysis
 - Myeloid cell sub-clustering
 - T cell sub-clustering
 - Label transfer using a reference
 - T cell trajectory
 - scTCR data processing
 - TCR analysis
- **QUANTIFICATION AND STATISTICAL ANALYSIS**
- **ADDITIONAL RESOURCES**

SUPPLEMENTAL INFORMATION

Supplemental information can be found online at <https://doi.org/10.1016/j.xcrm.2025.101973>.

Received: December 18, 2023

Revised: August 18, 2024

Accepted: January 22, 2025

Published: February 20, 2025

REFERENCES

1. Mehanna, J., Haddad, F.G., Eid, R., Lambertini, M., and Kourie, H.R. (2019). Triple-negative breast cancer: current perspective on the evolving therapeutic landscape. *Int. J. Womens Health* *11*, 431–437. <https://doi.org/10.2147/IJWH.S178349>.
2. Bianchini, G., De Angelis, C., Licata, L., and Gianni, L. (2022). Treatment landscape of triple-negative breast cancer — expanded options, evolving needs. *Nat. Rev. Clin. Oncol.* *19*, 91–113. <https://doi.org/10.1038/s41571-021-00565-2>.
3. Cortesi, L., Rugo, H.S., and Jackisch, C. (2021). An Overview of PARP Inhibitors for the Treatment of Breast Cancer. *Target. Oncol.* *16*, 255–282. <https://doi.org/10.1007/s11523-021-00796-4>.
4. Bardia, A., Hurvitz, S.A., Tolaney, S.M., Loirat, D., Punie, K., Oliveira, M., Brufsky, A., Sardesai, S.D., Kalinsky, K., Zelnak, A.B., et al. (2021). Sacituzumab Govitecan in Metastatic Triple-Negative Breast Cancer. *N. Engl. J. Med.* *384*, 1529–1541. <https://doi.org/10.1056/NEJMoa2028485>.
5. Zagami, P., and Carey, L.A. (2022). Triple negative breast cancer: Pitfalls and progress. *Targeted Oncol.* *8*, 95. <https://doi.org/10.1038/s41523-022-00468-0>.
6. El Bairi, K., Haynes, H.R., Blackley, E., Fineberg, S., Shear, J., Turner, S., de Freitas, J.R., Sur, D., Amendola, L.C., Gharib, M., et al. (2021). The tale of TILs in breast cancer: A report from The International Immuno-Oncology Biomarker Working Group. *npj Breast Cancer* *7*, 150. <https://doi.org/10.1038/s41523-021-00346-1>.
7. Thomas, R., Al-Khadairi, G., and Decock, J. (2020). Immune Checkpoint Inhibitors in Triple Negative Breast Cancer Treatment: Promising Future Prospects. *Front. Oncol.* *10*, 600573.
8. Cortés, J., Lipatov, O., Im, S.-A., Gonçalves, A., Lee, K.S., Schmid, P., Tamura, K., Testa, L., Witzel, I., Ohtani, S., et al. (2019). KEYNOTE-119: Phase III study of pembrolizumab (pembro) versus single-agent chemotherapy (chemo) for metastatic triple negative breast cancer (mTNBC). *Ann. Oncol.* *30*, v859–v860. <https://doi.org/10.1093/annonc/mdz394.010>.
9. Turiello, R., Pinto, A., and Morello, S. (2020). CD73: A Promising Biomarker in Cancer Patients. *Front. Pharmacol.* *11*, 609931.
10. Huang, S., Apasov, S., Koshiba, M., and Sitkovsky, M. (1997). Role of A2a extracellular adenosine receptor-mediated signaling in adenosine-mediated inhibition of T-cell activation and expansion. *Blood* *90*, 1600–1610.
11. Yang, R., Elsaadi, S., Misund, K., Abdollahi, P., Vandsemb, E.N., Moen, S.H., Kusnierczyk, A., Slupphaug, G., Standal, T., Waage, A., et al. (2020). Conversion of ATP to adenosine by CD39 and CD73 in multiple myeloma can be successfully targeted together with adenosine receptor A2A blockade. *J. Immunother. Cancer* *8*, e000610. <https://doi.org/10.1136/jitc-2020-000610>.
12. Antonioli, L., Pacher, P., Vizi, E.S., and Haskó, G. (2013). CD39 and CD73 in immunity and inflammation. *Trends Mol. Med.* *19*, 355–367. <https://doi.org/10.1016/j.molmed.2013.03.005>.
13. Ghalamfarsa, G., Kazemi, M.H., Raoofi Mohseni, S., Masjedi, A., Hojjat-Farsangi, M., Azizi, G., Yousefi, M., and Jadidi-Niaragh, F. (2019). CD73 as a potential opportunity for cancer immunotherapy. *Expert Opin. Ther. Targets* *23*, 127–142. <https://doi.org/10.1080/14728222.2019.1559829>.
14. Turcotte, M., Spring, K., Pommey, S., Chouinard, G., Cousineau, I., George, J., Chen, G.M., Gendoo, D.M.A., Haibe-Kains, B., Karn, T., et al. (2015). CD73 Is Associated with Poor Prognosis in High-Grade Serous Ovarian Cancer. *Cancer Res.* *75*, 4494–4503. <https://doi.org/10.1158/0008-5472.CAN-14-3569>.
15. Buisseret, L., Pommey, S., Allard, B., Garaud, S., Bergeron, M., Cousineau, I., Armeje, L., Bareche, Y., Paesmans, M., Crown, J.P.A., et al. (2018). Clinical significance of CD73 in triple-negative breast cancer: multiplex analysis of a phase III clinical trial. *Ann. Oncol.* *29*, 1056–1062. <https://doi.org/10.1093/annonc/mdx730>.
16. Loi, S., Pommey, S., Haibe-Kains, B., Beavis, P.A., Darcy, P.K., Smyth, M.J., and Stagg, J. (2013). CD73 promotes anthracycline resistance and poor prognosis in triple negative breast cancer. *Proc. Natl. Acad. Sci. USA* *110*, 11091–11096. <https://doi.org/10.1073/pnas.1222251110>.
17. Tu, E., McGlinchey, K., Wang, J., Martin, P., Ching, S.L., Floc'h, N., Kurawawa, J., Starrett, J.H., Lazdun, Y., Wetzel, L., et al. (2022). Anti-PD-L1 and anti-CD73 combination therapy promotes T cell response to EGFR-mutated NSCLC. *JCI Insight* *7*, e142843. <https://doi.org/10.1172/jci.insight.142843>.
18. Li, F., Li, C., Cai, X., Xie, Z., Zhou, L., Cheng, B., Zhong, R., Xiong, S., Li, J., Chen, Z., et al. (2021). The association between CD8+ tumor-infiltrating lymphocytes and the clinical outcome of cancer immunotherapy: A systematic review and meta-analysis. *eClinicalMedicine* *41*, 101134. <https://doi.org/10.1016/j.eclinm.2021.101134>.
19. Gueguen, P., Metrokidou, C., Dupic, T., Lawand, M., Goudot, C., Baulande, S., Lameiras, S., Lantz, O., Girard, N., Seguin-Givelet, A., et al. (2021). Contribution of resident and circulating precursors to tumor-infiltrating CD8+ T cell populations in lung cancer. *Sci. Immunol.* *6*, eabd5778. <https://doi.org/10.1126/sciimmunol.abd5778>.
20. Guo, X., Zhang, Y., Zheng, L., Zheng, C., Song, J., Zhang, Q., Kang, B., Liu, Z., Jin, L., Xing, R., et al. (2018). Global characterization of T cells in non-small-cell lung cancer by single-cell sequencing. *Nat. Med.* *24*, 978–985. <https://doi.org/10.1038/s41591-018-0045-3>.
21. Zheng, L., Qin, S., Si, W., Wang, A., Xing, B., Gao, R., Ren, X., Wang, L., Wu, X., Zhang, J., et al. (2021). Pan-cancer single-cell landscape of tumor-infiltrating T cells. *Science* *374*, abe6474. <https://doi.org/10.1126/science.abe6474>.
22. Siddiqui, I., Schaeuble, K., Chennupati, V., Fuertes Marraco, S.A., Calderon-Copete, S., Pais Ferreira, D., Carmona, S.J., Scarpellino, L., Gfeller, D., Pradervand, S., et al. (2019). Intratumoral Tcf1+PD-1+CD8+ T Cells with Stem-like Properties Promote Tumor Control in Response to Vaccination and Checkpoint Blockade Immunotherapy. *Immunity* *50*, 195–211. <https://doi.org/10.1016/j.immuni.2018.12.021>.

23. Sade-Feldman, M., Yizhak, K., Bjorgaard, S.L., Ray, J.P., de Boer, C.G., Jenkins, R.W., Lieb, D.J., Chen, J.H., Frederick, D.T., Barzily-Rokni, M., et al. (2018). Defining T Cell States Associated with Response to Checkpoint Immunotherapy in Melanoma. *Cell* 175, 998–1013. <https://doi.org/10.1016/j.cell.2018.10.038>.
24. Clarke, J., Panwar, B., Madrigal, A., Singh, D., Gujar, R., Wood, O., Chee, S.J., Eschweiler, S., King, E.V., Awad, A.S., et al. (2019). Single-cell transcriptomic analysis of tissue-resident memory T cells in human lung cancer. *J. Exp. Med.* 216, 2128–2149. <https://doi.org/10.1084/jem.20190249>.
25. Bassez, A., Vos, H., Van Dyck, L., Floris, G., Arijs, I., Desmedt, C., Boeckx, B., Vanden Bempt, M., Nevelsteen, I., Lambein, K., et al. (2021). A single-cell map of intratumoral changes during anti-PD1 treatment of patients with breast cancer. *Nat. Med.* 27, 820–832. <https://doi.org/10.1038/s41591-021-01323-8>.
26. Eisenhauer, E.A., Therasse, P., Bogaerts, J., Schwartz, L.H., Sargent, D., Ford, R., Dancey, J., Arbuck, S., Gwyther, S., Mooney, M., et al. (2009). New response evaluation criteria in solid tumours: revised RECIST guideline (version 1.1). *Eur. J. Cancer* 45, 228–247. <https://doi.org/10.1016/j.ejca.2008.10.026>.
27. Tirosh, I., Izar, B., Prakadan, S.M., Wadsworth, M.H., Treacy, D., Trombetta, J.J., Rotem, A., Rodman, C., Lian, C., Murphy, G., et al. (2016). Dissecting the multicellular ecosystem of metastatic melanoma by single-cell RNA-seq. *Science* 352, 189–196. <https://doi.org/10.1126/science.aad0501>.
28. Wu, S.Z., Al-Eryani, G., Roden, D.L., Junankar, S., Harvey, K., Andersson, A., Thennavan, A., Wang, C., Torpy, J.R., Bartonicek, N., et al. (2021). A single-cell and spatially resolved atlas of human breast cancers. *Nat. Genet.* 53, 1334–1347. <https://doi.org/10.1038/s41588-021-00911-1>.
29. Nalio Ramos, R., Missolo-Koussou, Y., Gerber-Ferder, Y., Bromley, C.P., Bugatti, M., Núñez, N.G., Tosello Boari, J., Richer, W., Menger, L., Denizeau, J., et al. (2022). Tissue-resident FOLR2+ macrophages associate with CD8+ T cell infiltration in human breast cancer. *Cell* 185, 1189–1207. <https://doi.org/10.1016/j.cell.2022.02.021>.
30. Angerer, P., Haghverdi, L., Büttner, M., Theis, F.J., Marr, C., and Buettner, F. (2016). destiny: diffusion maps for large-scale single-cell data in R. *Bioinformatics* 32, 1241–1243. <https://doi.org/10.1093/bioinformatics/btv715>.
31. Chen, Z., Ji, Z., Ngjoi, S.F., Manne, S., Cai, Z., Huang, A.C., Johnson, J., Staube, R.P., Bengsch, B., Xu, C., et al. (2019). TCF-1-Centered Transcriptional Network Drives an Effector versus Exhausted CD8 T Cell-Fate Decision. *Immunity* 51, 840–855. <https://doi.org/10.1016/j.immuni.2019.09.013>.
32. Bai, Y., Hu, M., Chen, Z., Wei, J., and Du, H. (2021). Single cell transcriptome analysis reveals RGS1 as a new marker and promoting factor for T cell exhaustion in multiple cancers. Preprint at bioRxiv. <https://doi.org/10.1101/2019.12.26.888503>.
33. Oliveira, G., Stromhaug, K., Klaeger, S., Kula, T., Frederick, D.T., Le, P.M., Forman, J., Huang, T., Li, S., Zhang, W., et al. (2021). Phenotype, specificity and avidity of antitumour CD8+ T cells in melanoma. *Nature* 596, 119–125. <https://doi.org/10.1038/s41586-021-03704-y>.
34. Cortes, J., Cescon, D.W., Rugo, H.S., Nowecki, Z., Im, S.-A., Yusof, M.M., Gallardo, C., Lipatov, O., Barrios, C.H., Holgado, E., et al. (2020). Pembrolizumab plus chemotherapy versus placebo plus chemotherapy for previously untreated locally recurrent inoperable or metastatic triple-negative breast cancer (KEYNOTE-355): a randomised, placebo-controlled, double-blind, phase 3 clinical trial. *Lancet* 396, 1817–1828. [https://doi.org/10.1016/S0140-6736\(20\)32531-9](https://doi.org/10.1016/S0140-6736(20)32531-9).
35. Schmid, P., Adams, S., Rugo, H.S., Schneeweiss, A., Barrios, C.H., Iwata, H., Diéras, V., Hegg, R., Im, S.-A., Shaw Wright, G., et al. (2018). Atezolizumab and Nab-Paclitaxel in Advanced Triple-Negative Breast Cancer. *N. Engl. J. Med.* 379, 2108–2121. <https://doi.org/10.1056/NEJMoa1809615>.
36. Miles, D., Gligorov, J., André, F., Cameron, D., Schneeweiss, A., Barrios, C., Xu, B., Wardley, A., Kaen, D., Andrade, L., et al. (2021). Primary results from IMpassion131, a double-blind, placebo-controlled, randomised phase III trial of first-line paclitaxel with or without atezolizumab for unresectable locally advanced/metastatic triple-negative breast cancer. *Ann. Oncol.* 32, 994–1004. <https://doi.org/10.1016/j.annonc.2021.05.801>.
37. Buisseret, L., Loirat, D., Aftimos, P., Maurer, C., Punie, K., Debien, V., Kristanto, P., Eiger, D., Goncalves, A., Ghiringhelli, F., et al. (2023). Paclitaxel plus carboplatin and durvalumab with or without oclumab for women with previously untreated locally advanced or metastatic triple-negative breast cancer: the randomized SYNERGY phase I/II trial. *Nat. Commun.* 14, 7018. <https://doi.org/10.1038/s41467-023-42744-y>.
38. Allard, B., Allard, D., Buisseret, L., and Stagg, J. (2020). The adenosine pathway in immuno-oncology. *Nat. Rev. Clin. Oncol.* 17, 611–629. <https://doi.org/10.1038/s41571-020-0382-2>.
39. Vigano, S., Alatzoglou, D., Irving, M., Ménétrier-Caux, C., Caux, C., Romero, P., and Coukos, G. (2019). Targeting Adenosine in Cancer Immunotherapy to Enhance T-Cell Function. *Front. Immunol.* 10, 925.
40. Alam, M.S., Kurtz, C.C., Rowlett, R.M., Reuter, B.K., Wiznerowicz, E., Das, S., Linden, J., Crowe, S.E., and Ernst, P.B. (2009). CD73 Is Expressed by Human Regulatory T Helper Cells and Suppresses Proinflammatory Cytokine Production and Helicobacter felis-Induced Gastritis in Mice. *J. Infect. Dis.* 199, 494–504. <https://doi.org/10.1086/596205>.
41. Facciabene, A., Motz, G.T., and Coukos, G. (2012). T Regulatory Cells: Key Players in Tumor Immune Escape and Angiogenesis. *Cancer Res.* 72, 2162–2171. <https://doi.org/10.1158/0008-5472.CAN-11-3687>.
42. Brambilla, E., Le Teuff, G., Marguet, S., Lantuejoul, S., Dunant, A., Graziano, S., Pirker, R., Douillard, J.-Y., Le Chevalier, T., Filipits, M., et al. (2016). Prognostic Effect of Tumor Lymphocytic Infiltration in Resectable Non-Small-Cell Lung Cancer. *J. Clin. Oncol.* 34, 1223–1230. <https://doi.org/10.1200/JCO.2015.63.0970>.
43. Kurtulus, S., Madi, A., Escobar, G., Klapholz, M., Nyman, J., Christian, E., Pawlak, M., Dionne, D., Xia, J., Rozenblatt-Rosen, O., et al. (2019). Checkpoint Blockade Immunotherapy Induces Dynamic Changes in PD-1-CD8+ Tumor-Infiltrating T Cells. *Immunity* 50, 181–194. <https://doi.org/10.1016/j.immuni.2018.11.014>.
44. Miller, B.C., Sen, D.R., Al Aboosy, R., Bi, K., Virkud, Y.V., LaFleur, M.W., Yates, K.B., Lako, A., Felt, K., Naik, G.S., et al. (2019). Subsets of exhausted CD8+ T cells differentially mediate tumor control and respond to checkpoint blockade. *Nat. Immunol.* 20, 326–336. <https://doi.org/10.1038/s41590-019-0312-6>.
45. Sj, I., M, H., My, G., J, L., Ht, K., Mc, B., Q, S., Js, H., J, L., Th, N., et al. (2016). Defining CD8+ T Cells That Provide the Proliferative Burst After PD-1 Therapy. *Nature* 537, 19330. <https://doi.org/10.1038/nature19330>.
46. Duhén, T., Duhén, R., Montler, R., Moses, J., Moudgil, T., de Miranda, N.F., Goodall, C.P., Blair, T.C., Fox, B.A., McDermott, J.E., et al. (2018). Co-expression of CD39 and CD103 identifies tumor-reactive CD8 T cells in human solid tumors. *Nat. Commun.* 9, 2724. <https://doi.org/10.1038/s41467-018-05072-0>.
47. Thommen, D.S., Koelzer, V.H., Herzig, P., Roller, A., Trefny, M., Dimeloe, S., Kialainen, A., Hanhart, J., Schill, C., Hess, C., et al. (2018). A transcriptionally and functionally distinct PD-1+ CD8+ T cell pool with predictive potential in non-small-cell lung cancer treated with PD-1 blockade. *Nat. Med.* 24, 994–1004. <https://doi.org/10.1038/s41591-018-0057-z>.
48. Zhang, Y., Chen, H., Mo, H., Hu, X., Gao, R., Zhao, Y., Liu, B., Niu, L., Sun, X., Yu, X., et al. (2021). Single-cell analyses reveal key immune cell subsets associated with response to PD-L1 blockade in triple-negative breast cancer. *Cancer Cell* 39, 1578–1593. <https://doi.org/10.1016/j.ccell.2021.09.010>.
49. Kazanietz, M.G., Durando, M., and Cooke, M. (2019). CXCL13 and Its Receptor CXCR5 in Cancer: Inflammation, Immune Response, and Beyond. *Front. Endocrinol.* 10, 471.
50. Schumacher, T.N., and Thommen, D.S. (2022). Tertiary lymphoid structures in cancer. *Science* 375, eabf9419. <https://doi.org/10.1126/science.abf9419>.
51. Liu, B., Zhang, Y., Wang, D., Hu, X., and Zhang, Z. (2022). Single-cell meta-analyses reveal responses of tumor-reactive CXCL13+ T cells to

- immune-checkpoint blockade. *Nat. Med.* 3, 1123–1136. <https://doi.org/10.1038/s43018-022-00433-7>.
52. van der Leun, A.M., Thommen, D.S., and Schumacher, T.N. (2020). CD8 + T cell states in human cancer: insights from single-cell analysis. *Nat. Rev. Cancer* 20, 218–232. <https://doi.org/10.1038/s41568-019-0235-4>.
53. Yost, K.E., Satpathy, A.T., Wells, D.K., Qi, Y., Wang, C., Kageyama, R., McNamara, K.L., Granja, J.M., Sarin, K.Y., Brown, R.A., et al. (2019). Clonal replacement of tumor-specific T cells following PD-1 blockade. *Nat. Med.* 25, 1251–1259. <https://doi.org/10.1038/s41591-019-0522-3>.
54. Yost, K.E., Satpathy, A.T., Wells, D.K., Qi, Y., Wang, C., Kageyama, R., McNamara, K.L., Granja, J.M., Sarin, K.Y., Brown, R.A., et al. (2019). Clonal replacement of tumor-specific T cells following PD-1 blockade. *Nat. Med.* 25, 1251–1259. <https://doi.org/10.1038/s41591-019-0522-3>.
55. Simoni, Y., Becht, E., Fehlings, M., Loh, C.Y., Koo, S.-L., Teng, K.W.W., Yeong, J.P.S., Nahar, R., Zhang, T., Kared, H., et al. (2018). Bystander CD8+ T cells are abundant and phenotypically distinct in human tumour infiltrates. *Nature* 557, 575–579. <https://doi.org/10.1038/s41586-018-0130-2>.
56. Wherry, E.J., and Kurachi, M. (2015). Molecular and cellular insights into T cell exhaustion. *Nat. Rev. Immunol.* 15, 486–499. <https://doi.org/10.1038/nri3862>.
57. Meysman, P., Barton, J., Bravi, B., Cohen-Lavi, L., Karnaukhov, V., Lille-skov, E., Montemurro, A., Nielsen, M., Mora, T., Pereira, P., et al. (2022). Benchmarking solutions to the T-cell receptor epitope prediction problem, IMMREP22 workshop report (Bioinformatics). <https://doi.org/10.1101/2022.10.27.514020>.
58. Gielis, S., Moris, P., Bittremieux, W., De Neuter, N., Ogunjimi, B., Laukens, K., and Meysman, P. (2019). Detection of Enriched T Cell Epitope Specificity in Full T Cell Receptor Sequence Repertoires. *Front. Immunol.* 10, 2820.
59. Montemurro, A., Schuster, V., Povlsen, H.R., Bentzen, A.K., Jurtz, V., Chronister, W.D., Crinklaw, A., Hadrup, S.R., Winther, O., Peters, B., et al. (2021). NetTCR-2.0 enables accurate prediction of TCR-peptide binding by using paired TCR α and β sequence data. *Commun. Biol.* 4, 1060–1113. <https://doi.org/10.1038/s42003-021-02610-3>.
60. Gianville, J., Huang, H., Nau, A., Hatton, O., Wagar, L.E., Rubelt, F., Ji, X., Han, A., Krams, S.M., Pettus, C., et al. (2017). Identifying specificity groups in the T cell receptor repertoire. *Nature* 547, 94–98. <https://doi.org/10.1038/nature22976>.
61. Dash, P., Fiore-Gartland, A.J., Hertz, T., Wang, G.C., Sharma, S., Souquette, A., Crawford, J.C., Clemens, E.B., Nguyen, T.H.O., Kedzierska, K., et al. (2017). Quantifiable predictive features define epitope specific T cell receptor repertoires. *Nature* 547, 89–93. <https://doi.org/10.1038/nature22383>.
62. Hao, Y., Hao, S., Andersen-Nissen, E., Mauck, W.M., Zheng, S., Butler, A., Lee, M.J., Wilk, A.J., Darby, C., Zager, M., et al. (2021). Integrated analysis of multimodal single-cell data. *Cell* 184, 3573–3587.e29. <https://doi.org/10.1016/j.cell.2021.04.048>.
63. Borcherdig, N., Bormann, N.L., and Kraus, G. (2020). scRepertoire: An R-based toolkit for single-cell immune receptor analysis. *F1000Res.* 9, 47. <https://doi.org/10.12688/f1000research.22139.2>.
64. Butler, A., Hoffman, P., Smibert, P., Papalexi, E., and Satija, R. (2018). Integrating single-cell transcriptomic data across different conditions, technologies, and species. *Nat. Biotechnol.* 36, 411–420. <https://doi.org/10.1038/nbt.4096>.
65. Ahlmann-Eltze, C., and Patil, I. (2021). ggsignif: R Package for Displaying Significance Brackets for “ggplot2.”. Preprint at PsyArXiv. <https://doi.org/10.31234/osf.io/7awm6>.
66. Bunis, D.G., Andrews, J., Fragiadakis, G.K., Burt, T.D., and Sirota, M. (2021). dittoSeq: universal user-friendly single-cell and bulk RNA sequencing visualization toolkit. *Bioinformatics* 36, 5535–5536. <https://doi.org/10.1093/bioinformatics/btaa1011>.
67. Amezcua, R.A., Lun, A.T.L., Becht, E., Carey, V.J., Carpp, L.N., Geistlinger, L., Marini, F., Rue-Albrecht, K., Rizzo, D., Soneson, C., et al. (2020). Orchestrating single-cell analysis with Bioconductor. *Nat. Methods* 17, 137–145. <https://doi.org/10.1038/s41592-019-0654-x>.
68. Lun, A., Riesenfeld, S., Andrews, T., Dao, T.P., Gomes, T., and participants in the 1st Human Cell Atlas Jamboree; and Marioni, J. (2019). EmptyDrops: distinguishing cells from empty droplets in droplet-based single-cell RNA sequencing data. *Genome Biol.* 20, 63. <https://doi.org/10.17863/CAM.40302>.
69. Korsunsky, I., Millard, N., Fan, J., Slowikowski, K., Zhang, F., Wei, K., Baglaenko, Y., Brenner, M., Loh, P.R., and Raychaudhuri, S. (2019). Fast, sensitive and accurate integration of single-cell data with Harmony. *Nat. Methods* 16, 1289–1296. <https://doi.org/10.1038/s41592-019-0619-0>.
70. Haghverdi, L., Büttner, M., Wolf, F.A., Buettner, F., and Theis, F.J. (2016). Diffusion pseudotime robustly reconstructs lineage branching. *Nat. Methods* 13, 845–848. <https://doi.org/10.1038/nmeth.3971>.

STAR★METHODS

KEY RESOURCES TABLE

REAGENT or RESOURCE	SOURCE	IDENTIFIER
Biological samples		
Human tumor fresh and frozen samples	Institut Curie, KU Leuven and Institut Bordet	N/A
Chemicals, peptides, and recombinant proteins		
CO2 Independent Medium	Gibco	15420604
DPBS	Gibco	14190144
Collagenase type I	Sigma-Aldrich	637958
Hyaluronidase	Sigma-Aldrich	H3506
Deoxyribonuclease	Sigma-Aldrich	D5025
UltraPure™ 0.5M EDTA, pH 8.0	ThermoFisher/Invitrogen	15575020
Bovine Serum Albumin	Roche	10711454001
Critical commercial assays		
EasySep™ Red Blood Cell (RBC) Depletion Reagent	STEMCELL Technologies	18170
EasySep™ Dead Cell Removal (Annexin V) Kit	STEMCELL Technologies	17899
EasyPlate™ EasySep™ Magnet	STEMCELL Technologies	18102
Chromium Next GEM Single Cell 5' Kit v2	10X Genomics	1000263
Chromium Single Cell Human TCR Amplification Kit	10X Genomics	1000252
High Sensitivity DNA kit	Agilent Technologies	5067–4626
Kapa Library Quantification kit	KAPA Biosystems	KK4828 – 07960166001
Deposited data		
scRNA-seq/scTCR-seq of 40 human tumor samples	This paper	EGAD50000000748
Software and algorithms		
Cell Ranger Single Cell Software Suite (v.6.1.5)	10X Genomics	https://support.10xgenomics.com/single-cell-gene-expression/software/pipelines/latest/installation
cellranger vdj (v.5.1.1)	10X Genomics	https://support.10xgenomics.com/single-cell-vdj/software/analysis-of-multiple-libraries/latest/lcb
Seurat (v.4.2.1)	Hao et al. ⁶²	https://satijalab.org/seurat/
scRepertoire (>v.1.7.0)	Borcherding et al. ⁶³	https://github.com/ncborcherding/scRepertoire
harmony (v.1.2.0)	Korsunsky et al. ⁶⁴	https://github.com/immunogenomics/harmony
ggsignif (v.0.6.4)	Ahlmann-Eltze et al. ⁶⁵	https://const-ae.github.io/ggsignif/
destiny (v.3.12.0)	Angerer et al. ³⁰	https://www.bioconductor.org/packages/release/bioc/html/destiny.html
dittoSeq (v.1.10.0)	Bunis et al. ⁶⁶	https://www.bioconductor.org/packages/release/bioc/html/dittoSeq.html
SingleCellExperiment (v.1.20.1)	Amezquita et al. ⁶⁷	https://www.bioconductor.org/packages/release/bioc/html/SingleCellExperiment.html

EXPERIMENTAL MODEL AND STUDY PARTICIPANT DETAILS

Study design

All patients were enrolled in the SYNERGY phase II trial (JJB-SYNERGY-012017; [NCT03616886](https://clinicaltrials.gov/ct2/show/study/NCT03616886)) an open-label, multicenter, randomized study in which previously untreated locally recurrent inoperable or metastatic TNBC patients received either weekly carboplatin (AUC 1.5) plus paclitaxel (80 mg/m²) × 12 and aPD-L1 (MEDI4736, durvalumab; 1500 mg q4w) (Arm B) ± aCD73 (MEDI9447, oleclumab; 3000 mg q2w × 5 then 3000 mg q4w) (Arm A). Both patients with PD-L1/CD73 positive or negative tumors were eligible. The primary objective of the study was to assess clinical benefit (CB) of oleclumab in combination with chemotherapy and durvalumab by the comparing the CB rate at 24 weeks between patients treated with or without the oleclumab. SYNERGY was conducted in accordance with the Declaration of Helsinki and the national regulatory requirements. All patients signed a written informed consent.

We initially profiled and collected data on 47 biopsy samples (including: 22 biopsy samples collected PRE-treatment, 23 biopsy samples collected ON-treatment (week 3), 1 biopsy collected ON-treatment (week 5) and 1 biopsy collected at progression status) derived from 29 TNBC patients (including 13 patients with matched PRE- and ON- treatment biopsies collected). Upon quality filtering of the scRNAseq data (based on the number of genes detected per each cell and the percent of mitochondrial gene expression; <15%) we removed from the final analysis 7 samples that had <150 cells. Therefore, in the final analysis included in this study we include: 40 biopsy samples, derived from 27 patients, including 12 patients with matched PRE- and ON- biopsy samples. 15 out of 27 patients were randomized to Arm A and 12 patients were randomized to Arm B. Tissue biopsies from a total of 27 patients were obtained via core needle biopsy at two timepoints: pre-treatment (week 0/baseline) and at on-treatment (week 3). For 12 out of the 27 patients paired-biopsy samples were obtained (from both pre- and on-treatment timepoints). 15 out of 27 patients to arm A; 12 out of the 27 patients were randomized to arm B. For 1 patient, on-treatment biopsy was collected at week 5 on treatment due to logistical constraints. For 1 patient with disease progression one additional tissue biopsy was collected at a later, progression timepoint.

Human specimens

Tissue biopsies from patients included in Institut Curie, Institut Jules Bordet and KU Leuven were obtained via a diagnostic biopsy needle. Samples were stored in CO₂-independent medium (Gibco) with 2% human serum and transferred within a period of -1h to the research institute. All 40 biopsy samples included in the current study were processed fresh, immediately upon surgical removal, with the exception of the following 5 samples: Baseline_P26, Baseline_P25, Week 3_P23, Week 3_P24, Week3_P27, which were initially frozen.

METHOD DETAILS

Biopsy tissue dissociation

Biopsy tissue samples were gently cut in about 0.5 mm³ pieces using scalpter. Tissues were digested enzymatically by a 20 min incubation, at 37°C under agitation, in CO₂-independent medium (Gibco) with collagenase I (2 mg/mL; # 637958; Sigma-Aldrich), hyaluronidase (2 mg/mL; #H3506; Sigma-Aldrich), and deoxyribonuclease (25 μg/ml; #D5025; Sigma-Aldrich). The tissue pieces were gently triturated with a 20mL syringe plunger on a 70um cell strainer (BD) in 1X PBS (Gibco) with 1% fetal bovine serum (FBS) and 2mM EDTA (Invitrogen) until uniform cell suspensions were obtained. The suspended cells were subsequently centrifuged for 10 min at 300 g at 4°C.

Red blood cell and dead cell removal

Red blood cells and dead cells were removed using magnetic isolation kit by StemCell technologies, following manufacturer instructions (Product numbers: #18170RF and #17899 respectively). Upon purification, cells were resuspended in the proper volume of 1X PBS with 0.04% BSA, based on the targeted cell recovery indicated by 10X Genomics. Cell numbers and viability were measured using a Countess II Automated Cell Counter (Thermo Fisher Scientific) and hemocytometer/trypan blue.

Sc-RNA-seq and TCR-seq profiling

Single-cell suspensions were loaded onto a Chromium Single Cell Chip (10X Genomics) according to the manufacturer's instructions for co-encapsulation with barcoded gel beads at a target capture rate of 1,000 to 10,000 individual cells per sample, based on the initial number of cells. For all samples RNA and TCR libraries were synthesized by following the Chromium Single Cell 5' V(D)J Enrichment Kit, Human T cell (10X Genomics). cDNA before and after TCR enrichment was profiled using both Qubit (ThermoFischer scientific) and Bioanalyzer High Sensitivity DNA kit (Agilent Technologies). Libraries for RNA-seq and V(D)J were prepared following the manufacturer's user guide (10X Genomics), then profiled using Kapa Library Quantification kit (Kapa Biosystems) and quantified with Qubit (Thermo Fisher Scientific) and TapeStation (Agilent Technologies). Single-cell RNA-seq libraries and TCR V(D)J libraries were sequenced with Novaseq (Illumina). All sequencing was done according to the manufacturer's specification (10X Genomics).

scRNA data processing

Single-cell expression was analyzed using the Cell Ranger Single Cell Software Suite (10X Genomics, v6.1.5) to perform quality control, sample demultiplexing, barcode processing, and single-cell 5' gene counting. Sequencing reads were aligned to the GRCh38

human reference genome (Ensembl 84) and quantified using cellranger count function. Filtered gene barcodes matrices, containing barcodes with UMI counts passing threshold for cell detection, were used for further analysis. Empty droplets removal was performed by the EmptyDrops package,⁶⁸ implemented in CellRanger.

Principal component analysis (PCA), UMAP clustering & downstream analysis

Downstream analysis was performed using Seurat⁶² (version 4.2.1). Quality control was performed to exclude cells with less than 200 or more than 6000 detected genes and with greater than 15% mitochondrial RNA content, with 76,079 cells passing these filters.

For cell clustering, raw UMI counts were log normalized and variable genes called on each dataset independently. The top 6000 variable features were identified using the “vst” method from Seurat. Variable T cell receptor and immunoglobulin genes were removed from the list of variable genes to prevent clustering based on variable V(D)J transcripts. To correct batch effects between samples, we used the reciprocal PCA (rPCA) integration method. This method is based on leveraging closely-related cells (termed anchors) between datasets, projection of each dataset into the others PCA space and construction of the anchors by the same mutual neighborhood requirement. Cell cycle score for S and G2/M cell cycle phase was assigned to each cell, based on previously published datasets²⁷ using the CellCycleScoring function.

Scaled scores for each gene were calculated using the Scale Data function and regressed against number of UMIs per cell and mitochondrial RNA content. Scaled data was used as an input into PCA based on variable genes. A stressed-induced cluster of low-quality cells (highly expressing mitochondrial/MT- and heat-shock/HSP- genes) was removed from the initial analysis and cells were re-analyzed. Clusters were identified based on the shared nearest neighbor (SNN) clustering on the first 14 PCs and resolution = 0.5. Principal components were used to generate UMAP projections. Unique cluster-specific differentially expressed genes were identified by performing the Seurat FindAllMarkers function using Wilcoxon test on the RNA assay. Signature scores were computed using the Seurat function AddModuleScore using the gene signature of interest and setting the number of control genes from the same bin of expression at 5. This function calculates for each individual cell the average expression of each gene signature, subtracted by the aggregated expression of control gene sets matched for individual gene expression level. For visualization of cluster numbers distribution barplots downstream analysis we used the dittoseq package (v.1.10.0).⁶⁶

Myeloid cell sub-clustering

For myeloid cell specific clustering, we isolated myeloid cell cluster from the general object (of [Figures 1 and 2](#)), containing all the broad clusters. To correct batch effects between samples, we used the harmony⁶⁹ integration method applied on the RNA assay of the selected samples. Variable genes were called on the RNA assay of the myeloid cell dataset independently and PCA was performed based on the variable gene set. Myeloid cell clusters were identified using SNN-based clustering based on the first 12 PCs with resolution = 0.5. Principal components were used to generate UMAP projections. Progression_P19 sample collected at later timepoint was excluded from the analysis. Samples with <50 total myeloid cells were excluded from further analysis (abundancies quantification), including: Baseline_P26, Baseline_P13, Baseline_P15, Baseline_P16, Baseline_P18, Baseline_P22, Baseline_P5, Week3_P15, Week3_P16, Week3_P17, Week3_P18, Week3_P24, Week3_P8, Week5_P22.

T cell sub-clustering

For T cell specific clustering, we isolated the T (NK) cell cluster from the general object (of [Figures 1 and 2](#)), containing all the broad clusters. Variable genes were called on the RNA assay of the T cell dataset independently and PCA was performed based on the variable gene set. T cell clusters were identified using SNN-based clustering based on the first 12 PCs with resolution = 0.8. Principal components were used to generate UMAP projections. Progression_P19 sample collected at later timepoint was excluded from the analysis. Baseline_P26 sample was excluded from further analysis (abundancies quantification), due to low cell number.

Label transfer using a reference

Label transfer was performed using Seurat v3 FindTransferAnchors and TransferData functions. FindTransferAnchors function identifies a set of anchors between a reference and query object and next TransferData function uses the set of anchors computed to transfer categorical or continuous data from the reference to the query object. Cycling cells cluster together due to co-expression of cell cycle genes. To identify their identity, label transfer method was used to assign the cells from the cycling cluster into their cluster-of-origin on the broad cluster UMAP and on the T cell cluster UMAP ([Figure 2F](#); [Figure S2D](#); [Figure 4D](#); [Figure S4E](#)).

T cell trajectory

For reconstruction of the continuum of the T cell differentiation analysis we used the diffusion pseudotime analysis as implemented in the destiny package (v.3.12.0).³⁰ In short Diffusion Pseudo Time (DPT) is a pseudo time metric based on the transition probability of a diffusion process.⁷⁰ We used the DiffusionMap() function in the destiny package on S4 T cell object generated using the as.SingleCellExperiment function in the SingleCellExperiment package (v.1.20.1).⁶⁷

scTCR data processing

TCR reads were aligned to the GRCh38 reference genome and consensus TCR annotation was performed using cellranger vdj (10X Genomics, version 5.1.1). TCR data were collected for $n = 36$ out of the 40 biopsy samples, due to technical issues ([Table S1](#)). TCR

annotation was performed using the 10X cellranger vdj pipeline. If more than one β chain was detected in a cell, then cell was considered as doublet and was excluded from further analysis. scRepertoire package⁶³ was used for clonotypes assignment and analysis of the clonotype dynamics.

TCR analysis

TCR analysis was performed for 36 out of the 40 total biopsy samples included in the study. TCR analysis shown in: Figures 6A and 6B, 6D, 6F-6G; Figure S6B, S6D-S6F, S6H; Figure 7 and Figure S7, was performed in all cells recovered per biopsy sample. TCR analysis shown in Figures 6C and 6E and Figures S6B-S6C, was performed on a downsampled-equal number of cells ($n = 78$) per biopsy sample. Mean clonotype size computed as the ratio between the total number of cells in the sample and the total number of unique clonotypes was used as a metric of clonal expansion. This metric was chosen for the analysis as it is the most appropriate for small sample size. To avoid bias from different sample size, computational downsampling procedure was performed by random selection of $n = 78$ cells from each sample (the value of 78 cells were chosen to include of maximum number of available samples to the analysis while having sufficient number of cells for expansion quantification). Random downsampling to 78 cells was performed 100 times for each sample and the average value of mean clonotype size was calculated.

For TCR clonotype sharing analysis we considered only patients for which paired samples PRE- and ON-treatment were available (responders: $N = 6$ patients, non-responders: $N = 5$ patients). A clonotype was considered as shared if it was detected in both time points (PRE- and ON-treatment) on the same patient.

As a metric of clonal sharing between timepoints, we used Jaccard index computed as

$$J(p) = \frac{\sum_i \min(N_i^{PRE}, N_i^{ON})}{\sum_i \max(N_i^{PRE}, N_i^{ON})}$$

where summation is carried out across all the unique clonotypes i detected in patient p ; N_i^{PRE} and N_i^{ON} correspond to number of times clonotype i is detected in PRE- and ON-treatment time points.

QUANTIFICATION AND STATISTICAL ANALYSIS

For comparison of cluster frequencies between patient groups (R vs. NR; PRE-vs. ON-treatment) statistical differences were assessed using two-way analysis of variance (ANOVA) test (in the case of comparison across more than two groups) or t-test (in the case of comparison of means between two groups). Analysis was performed using Prism 8; GraphPad Software, version 8.4.2. When we compare multiple parameters across multiple groups (two-way ANOVA) a multiple comparison testing correction was applied and adjusted p -values were reported.

In violin plot and barplot representations (see Figure 4E; Figure 5D; Figure S5F), t-tests were performed to compare mean gene signature expression between the different CD8⁺ clusters (paired t-test) and in R vs. NR patients, PRE-vs. ON-treatment (unpaired t-test) using R package ggsignif⁶⁵ (version 0.6.4); p -values: ns: p -value > 0.05 ; * p -value ≤ 0.05 ; ** p -value ≤ 0.01 ; *** p -value ≤ 0.001 ; **** p -value ≤ 0.0001 . Samples were treated as pseudobulks using the AggregateExpression() function of Seurat package. Differential expression analysis (as shown in Figures 5E and 5F) was performed on samples treated as pseudobulks using the AggregateExpression() function of Seurat package, with red dot denoting significant individual genes with adj p -value < 0.05 and fold change > 0.25 .

ADDITIONAL RESOURCES

Samples analyzed in the current study derived from patients enrolled in the SYNERGY phase II trial, description: <https://clinicaltrials.gov/study/NCT03616886>.